QUANTUM INFORMATION APPLICATIONS OF FREQUENCY UPCONVERSION

BY

AARON PACE VANDEVENDER

S.B., Massachusetts Institute of Technology, 2001

DISSERTATION

Submitted in partial fulfillment of the requirements
for the degree of Doctor of Philosophy in Physics
in the Graduate College of the
University of Illinois at Urbana-Champaign, 2007

Urbana, Illinois

Abstract

We demonstrate the utility of frequency upconversion in a non-linear crystal for quantum information applications. By combining a bright "escort" beam with a signal photon inside of a periodically poled lithium niobate (PPLN) crystal, we are able to achieve near unit conversion efficiency. We use this conversion process to create high-efficiency infrared single-photon detectors by upconverting infrared photons to visible ones and using efficient silicon avalanche photo diodes to detect the upconverted photon. We have achieved a net system detection efficiency of 56%, far superior to previous methods for infrared photon detection.

We also demonstrate the phase coherence of the upconversion process, which enables it to convert photonic qubits from one wavelength to another, potentially allowing quantum networks of disparate operating wavelengths to communicate efficiently. This quantum "transduction" feature is observed by upconverting photons passed between two unbalanced Michelson interferometers that create and measure time-bin qubits, similar to those used in many quantum cryptography systems, and verifying that the phase of the qubits is preserved.

The Rabi oscillation-like behavior of upconversion is also demonstrated, allowing for the creation and manipulation of highly non-degenerate frequency qubits. These states may be used in conjunction with other degrees of freedom such as polarization, time-bin, or orbital angular momentum states to enlarge the usable single-photon Hilbert space and create a rich vocabulary for transmission of quantum information.

To Cosmic Ray.

Acknowledgments

Funding for this work has been graciously provided by the ARO, DTO, and the MURI Center for Photonic Quantum Information System (ARO/DTO program DAAD19-03-1-0199). Thanks to my parents, Pace and Nancy VanDevender, my teachers, Raymond Menegus, Alexander Kupershtokh, and Selim Shahriar, and my adviser Paul G. Kwiat.

Table of Contents

List of Tables . . . . . **viii**

List of Figures . . . . . **ix**

List of Abbreviations . . . . . **xiv**

1 Introduction **1**
1.1 Upconversion Background 2
1.2 Periodic Poling 4
1.3 Experiments on Upconversion 5

2 Numerical Modeling **7**
2.1 Simulation Introduction 7
2.2 Field Evolution Approximations 7
2.3 Phasematching 10
2.4 High-Efficiency Tolerances 12

3 Detection **17**
3.1 Detection Introduction 17
3.2 Upconversion Detector Overview 18
3.3 Escort Delay 19
3.4 Escort Attenuation 21
3.5 Input Pulse Generation 22
3.5.1 Input Pulse Verification 25
3.5.2 Bias Control 27
3.6 Mode Alignment 29
3.7 Low-Loss Filtering 31
3.8 Efficiency Results 32

4 Coherent Upconversion **33**
4.1 Coherence Introduction 33
4.2 Experimental Setup 34
4.3 Coherence Results 37

5 Rabi Oscillations **41**
5.1 Introduction 41
5.2 Theory of Photon Rabi Oscillations 41
5.3 Indirect Observations of Photon Rabi Oscillations 42
5.4 Direct Observations of Rabi Oscillations 45
5.5 Atom Simulator 47

6 Upconversion Switching 51
6.1 Introduction 51
6.2 Theory of Upconversion Phase Modulation 51
6.3 Mach-Zehnder Switch 52
6.4 Polarization Switch 52
6.5 Frequency Multiplexing 55
6.6 Bias-Free Sagnac Switch 56
6.7 Other Implementations 57

A upconversion.scm 59

B process-pulse.scm 64

C error-analysis.scm 67

D Noise from Crystal Damage 69

References 72

Author's Biography 75

List of Tables

5.1 Timing chronology in indirect Rabi observation 46

List of Figures

1.1 a) Feynman diagrams of the upconversion and downconversion processes. During upconversion, a photon with frequency ω_i combines with a photon of frequency ω_e to produce a photon of frequency $\omega_o = \omega_i + \omega_e$. Downconversion splits the high-frequency photon (ω_o) to produce two daughter photons (ω_i and ω_e). b) Pulse sequences for the upconversion process. An escort pulse is combined with a continuous signal beam in a $\chi^{(2)}$ nonlinear crystal. The escort is unchanged, while the signal that overlaps the escort is depleted and a pulse is generated at the output frequency. 1

2.1 Electric field vs. position in the crystal for the poled and non-poled cases. 8
2.2 Output light predicted for 1-mW input power, 10-kW escort power, using exact numerical model and numerical model with non-depletion and quasi-phasematched approximations. The final output of the approximated model is 0.2% higher than the exact model. 9
2.3 Calculated phasematching crystal poling period at operating temperature (solid) and at 25 °C (dashed) versus a given operating temperature. The graphs are sufficiently similar, so we can safely ignore the effects of thermal expansion when designing our system. 10
2.4 Phasematched escort wavelength versus input wavelength for the different models of dispersion: zero local dispersion, linear dispersion, and the full Sellmeier dispersion equation. The poling period and temperature are held constant at 11.4 μm and 94.8 °C, respectively. 11
2.5 Phasematching temperature for a range of wavelengths. The escort wavelength is held constant at 1064 nm and the poling period is assumed to be 11.4 μm. 12
2.6 Predicted conversion efficiency for fixed wavelengths over a range of poling periods. Input and escort wavelengths are 1550 and 1064 nm, crystal length is 22 mm, temperature was 92 °C, and the escort power was 1 kW with a 177-μm spot size. 13
2.7 Predicted conversion efficiency over a range of temperatures. . . 14
2.8 Predicted conversion efficiency over a range of input wavelengths. 15
2.9 Width of the temperature tuning curve (Figure 2.7) for various crystal lengths. 15
2.10 Width of the input wavelength tuning curve (Figure 2.8) for various crystal lengths. 16

2.11 Predicted conversion efficiency vs. 1550-nm input pulse width. 1550-nm light is upconverted using a 1064-nm 600-ps escort pulse. If the input pulse is too long, the temporal overlap is reduced, lowering efficiency. If the pulse is too short, the spectral width of the pulse becomes very wide, inhibiting phasematching and reducing efficiency. 16

3.1 High efficiency upconversion experiment. A weak 1550-nm pulse is combined on a dichroic beam splitter (DBS) with a bright 1064-nm escort pulse and focused into a non-linear crystal (PPLN). The 631-nm upconverted pulse is then filtered through dispersion prisms and an interference filter, and finally detected by a silicon Avalanche Photodiode (APD). 18
3.2 Oscilloscope trace of escort laser. The JDS Uniphase DNP-150010-000 DualChip NanoPulse Laser generates ∼600-ps pulses at 1064 nm with a repetition rate of 44.1 kHz. The trace was taken using an EOT InGaAs PIN photodiode (EOT model ET-3500F) connected to an HP Agilent 81000FA Signal Analyzer Mainframe. 19
3.3 Power of converted light is plotted against input power. The overall conversion efficiency is low due to the low duty cycle of the escort laser (600-ps pulses at 7.2 kHz), since the input beam was CW, the escort was pulsed, and only the input light coincident with an escort pulse. The data show the conversion process is highly linear over several orders of magnitude. The lowest-power point on the graph was measured using a silicon APD single-photon counter, while the other points were measured using a Newport 818-SL Power Meter. 20
3.4 Diagram of a Harriot cell delay line with "time reversal" mirror. A horizontally polarized beam enters though a 5-mm hole in a curved mirror, bounces several times between the two curved mirrors, and exits a hole in the opposite mirror. It is then partially rotated by a quarter waveplate (QWP), focused with a lens, and reflected at the focal point by the mirror. It then retraces its path backwards, rotating to vertical polarization, and again bouncing several times on the curved mirrors. Finally it reflects off of the polarizing beamsplitter (PBS), having been delayed some ∼200 ns. 21
3.5 Timing jitter of the input pulse driver system is measured at 82 ps. We used the escort laser to create trigger pulses on two identical AEPX-65 fast photodiodes. The signal from the first diode is used to trigger the input pulse driver system, which is then used to start a time-to-amplitude converter (TAC), while the second diode signal–which is optically delayed from the first using the Harriot cell delay line (Figure 3.4)–is used to stop the TAC. We count the TAC pulses on a multichannel analyzer (MCA) and from the resulting distribution obtain the input pulse jitter. . . . 23
3.6 Comparison of the original oscilloscope trace of the input pulse with the post-processed pulse waveform. The post-processing removes detector offset, high-frequency noise, and systematic ringing in the detector, thereby providing a much more accurate estimate of the actual pulse shape. 25

3.7 Measurement and fit of the error of pulse-area measurements as a function of integration time interval. Error originates from two sources: shot-to-shot systematic error and linear drift of v_0, the voltage required to balance the modulator. We find the former error dominates for times under 40 ps, while the latter dominates for longer time windows. 26
3.8 Bias feedback control circuit for electrooptic modulator. A 1-kHz dither signal modulates the bias voltage of an EOM. The resulting 2-kHz photo-signal is modulated with the 1-kHz clock and averaged over 120 ms to determine if the current bias is too high or low. The signal is then fed back into the integrator, which maintains the bias with the correct feedback sign (positive or negative), determined by a switching inverter to maintain minimum or maximum EOM transmission. 27
3.9 Numerical model of feedback dependence of the bias control circuit, with $v_0 = 2$ V and $v_\pi = 5$ V. We observe that when v_{in} is greater (less) than v_0 the feedback is positive (negative). 28
3.10 Circuit for amplifying and protecting the diode [1]. The feedback on the operational amplifier is configured to maintain the voltage across the diode at 0 V, independent of the photo current passing through the diode. The signal output is highly linearly related to the intensity of light incident on the diode, improving the feedback circuit responsiveness. 29

4.1 a) A 1550-nm pulse is prepared along with a bright 1064-nm escort pulse in a two-time-bin superposition state using an unbalanced Mach-Zehnder interferometer. The photon is upconverted and then passed through another interferometer with a phase shifter in one arm. Interference fringes are observed in the resulting middle time-bin. b) An equivalent, but more robust, implementation using an unbalanced Michelson interferometer. After the two time-bin state is prepared and upconverted, it is reflected back through the interferometer, and picked off using a dichroic beam splitter where it is detected by an APD. Lenses in the arms focus onto flat end mirrors, effectively time reversing the beam. A dispersive glass plate is tipped to control the phase between long-short and short-long processes. c) Curved mirrors at the ends of each arm are used to time-reverse the beam, and the single glass plate is replaced by two dispersive glass plates that are tipped near Brewster's angle to produce a low-loss and zero-walkoff phase shift between the long-short and short-long processes. 35
4.2 Coherence fringes along with a fit of the fringes. The fit was based on a calculation of the phase induced by tilting a microscope slide of known thickness and dispersion function. The fit has only two free parameters, the visibility and the initial phase. Though the overall character of the fit is confirmed, the counts fluctuate more than we would expect from counting statistics. We attribute this to nonuniformity in the microscope slide. 38

4.3 a) Detected photons versus time for two settings of the phase glass, corresponding to constructive and destructive interference. The long-long and short-short processes are unaffected by the position of the phase glass, while the central time-bin, arising from the interfering short-long and long-short processes, varies greatly. b) Number of photons detected in the central time bin as the phase glass plates are tilted. The 95%-visibility fringe demonstrates the coherence of the upconversion process. 40

5.1 Analog sampling oscilloscope trace of the 7.2-kHz 1064-nm 50-mW Nd:YAG laser (JDS Uniphase NP-00321-110) along with a fit. The fit function used is a Gaussian pulse with an exponential tail. 43
5.2 Oscilloscope trace of a 1550-nm laser pulse that was shaped by passing the light from a CW 1550-nm telecommunications fiber-coupled laser diode through an electrooptic modulator driven by an Avtech electrical pulse generator. 44
5.3 Layout of the scheme of indirect Rabi oscillation measurements. The solid lines represent electrical signals, while the dashed lines are laser beam paths. An escort and an input pulse are applied to the crystal with a random relative delay between the pulses. When we fail to detect an upconverted photon for a particular pulse, that delay is recorded and a histogram (Figure 5.4) is made, showing the relative probability that a delay will *not* result in an upconverted photon. 45
5.4 Indirect measurement of Rabi oscillations. Escort pulse shape along with its theoretical conversion profile obtained from a 400-ps input pulse. We record the relative input-escort delay of pulses that generated upconverted photons (calculated from subtracting events which did *not* upconvert from the background). This measurement is equivalent to the probability of conversion as the input pulse is swept across the escort pulse, and should be similar to the plotted theoretical prediction. The asymmetry of the data is likely due to a long escort tail which was not accounted for in the theoretical model of the escort. However, the salient feature of the graph–the two peaks–is present, indicating that overconversion is achieved. 47
5.5 The Rabi oscillation-like nature of upconversion (Eqn. 1.9) is demonstrated by measuring the rate of upconverted photons for increasing escort-pulse intensities. The imperfect visibility is well modeled (solid line) by the precise pulse shapes. Visibility is mostly limited by the extent to which the 1544-nm pulse is temporally and spatially smaller than the escort pulse. The prediction was scaled in the pulse-energy direction due to inability to measure the absolute peak escort intensity to better than a factor of 2; however, predicted and measured pulse energies agree to that level. 48
5.6 Dependence of phasematched escort and output wavelengths vs. input wavelength for constant crystal poling period (here assumed to be $\Lambda = 11.4$ μm). The output wavelength curve is plotted on an axis that is merely shifted and not scaled from the escort curve. This is to illustrate the relatively flat dependence of the output curve as compared to the escort curve. 49

5.7 Multiple overlapping Rabi oscillations can be used to model the dynamics of a multilevel atom. Several pairs of input and escort wavelengths simultaneously phasematch with a single output wavelength. The escort beams act on the input beams as driving radiation fields act on the electronic structure of an atom. The input wavelengths are analogous to the excited states of the atom, while the output state is analogous to the ground state. By combining various escort wavelengths in a single crystal, we can create photons in complex nondegenerate superposition states. 50

6.1 Design of basic upconversion switch using a Mach-Zehnder interferometer. A signal laser beam is sent through a balanced interferometer with a non-linear crystal (e.g., PPLN) in one arm. When an escort beam is passed through the crystal, collinearly with the signal, a π-phase shift is acquired by the signal, switching it from Port 1 to Port 2. 52
6.2 A diagonally polarized signal is passed through a non-linear crystal phase-matched for upconversion with an escort laser. The signal is filtered, and then passed though two waveplates and a PBS so that it exits out Port 1. When the escort beam is turned on, a π-phase shift is applied to the vertical component of the signal, switching it from Port 1 to Port 2. 53
6.3 Data collected from the polarization-based upconversion switch. A 1544-nm signal was modulated with a 600-ps wide 1064-nm pulse in 4.5-cm PPLN crystal. The extinction is $\sim$20 dB and the transmission is about 70%. To average out the noise on the photodetector, each trace is a composite of 16 escort pulses. . . . 54
6.4 Data showing the wavelength selectivity of the upconversion switch, which therefore allows for frequency multiplexing. A 4.5-cm PPLN crystal and a 0.15-nm wide escort produce a 0.3-nm wide acceptance bandwidth. Nearby frequencies are unaltered. Transparency is limited to about 80% due to imperfect modematching between the escort and the signal. 56
6.5 Design of bias-free upconversion switch using a Sagnac design. Since only the signal co-propagating with the escort beam acquires a phase, modulating the escort beam will shift the interference of the interferometer at the beam splitter and control whether the signal exits at Port 1 or Port 2. 58

D.1 Photo taken under a microscope of the end of a damaged PPLN crystal. The discoloration of the first $\sim$1 mm is evident. 70
D.2 Measurement of noise versus polarization. A fit reveals a polarization visibility of 93%, and is horizontally polarized. 70
D.3 Measurement of noise versus lateral position in the crystal. The noise peaks near the 11.4-μm channel that we use for upconversion. From this, it seems likely that the presence of the intense escort beam contributed to causing the damage, possibly through burning or photo-refractive damage. 71
D.4 Measurement of noise versus power. The fit shows a quadratic dependence on escort power, until the detector saturates near the pulse repetition rate at 44 kHz. The fit function is $N = 4200(1 - \exp(1.8I^2))$, where N is the number of background counts per second, and I is the fraction of maximum escort power used. . . 71

List of Abbreviations

APD	Avalanche Photodiode
CFD	Constant Fraction Discriminator
EOM	Electrooptic Modulator
DWDM	Dense Wave-Division Multiplexing
FWHM	Full Width at Half Maximum
HWP	Half Waveplate
InGaAs	Indium Gallium Arsenide
IR	Infrared
MCA	Multichannel Analyzer
PBS	Polarizing Beam Splitter
PLD	Proportional-Integral-Differential
PPLN	Periodically Poled Lithium Niobate
QKD	Quantum Key Distribution
QWP	Quarter Waveplate
TAC	Time-to-Amplitude Converter
YAG	Yttrium Aluminum Garnet

1 Introduction

Since the prediction by Armstrong et al. [2] that multiple optical wavelengths could be mixed using non-linear dielectric media, frequency upconversion [3] has been successfully used in a wide variety of classical optical applications, including narrow-band infrared (IR) imaging [4], black-body thermal imaging [5], and IR [6] and time-resolved [7] spectroscopy, as well as detection of sources from the near IR (e.g., 1550 nm) to the very deep IR [8] (e.g., 10.6 μm). The techniques may also be employed in improved single-molecule detection [9] and low-light IR astronomy [10].

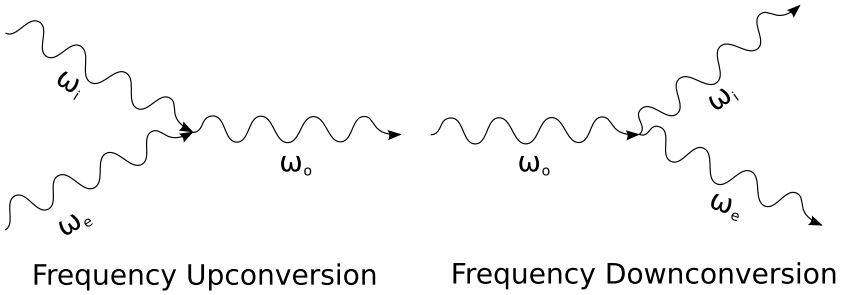

a)

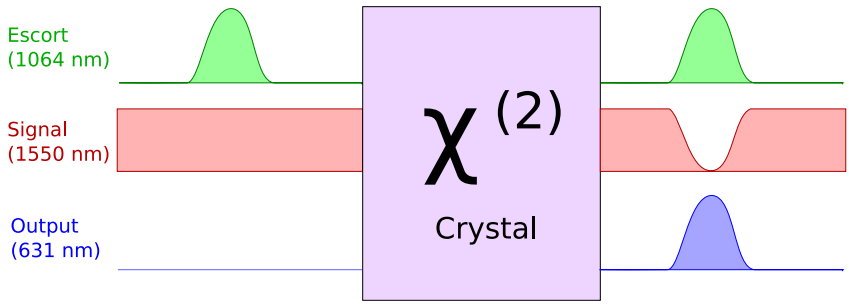

b)

Figure 1.1: a) Feynman diagrams of the upconversion and downconversion processes. During upconversion, a photon with frequency ω_i combines with a photon of frequency ω_e to produce a photon of frequency $\omega_o = \omega_i + \omega_e$. Downconversion splits the high-frequency photon (ω_o) to produce two daughter photons (ω_i and ω_e). b) Pulse sequences for the upconversion process. An escort pulse is combined with a continuous signal beam in a $\chi^{(2)}$ nonlinear crystal. The escort is unchanged, while the signal that overlaps the escort is depleted and a pulse is generated at the output frequency.

Now frequency upconversion, the process of combining two photons in a nonlinear medium to produce a third, higher-energy photon (See Figure 1.1), promises to enhance and enable several quantum information technologies where the promise of optical qubits is greatly enriched by the ability to shift their wavelengths to desired values [11, 12, 13, 14, 15, 16]. For example, high-efficiency single-photon detectors which utilize frequency upconversion of telecommunication-wavelength photons could substantially increase the range and data rates of quantum cryptography systems that rely on faithfully transmitting and receiving IR single-photon quantum states [17]. Upconversion may also be used to prepare complex quantum states by partially upconverting a photon into an arbitrary superposition of two frequencies. This, in addition to polarization, angular momentum, and time-bin, provides another degree of freedom for transmitting quantum information. Finally, future quantum networks will likely require the ability to freely change between the wavelength of a particular "flying" qubit (e.g., a telecommunication-wavelength photon) and a "stationary" qubit (e.g., a trapped atom or quantum dot). This type of quantum "transduction" may have an important role in distributed quantum computation [18] and quantum communication [19].

In order for upconversion to be suitable for use in these applications, however, two properties must be demonstrated. First, the process must be efficient at the single-photon level—we must have the capability to convert nearly all of one frequency to another frequency reliably and with low loss. Here we demonstrate a high-efficiency frequency upconversion process from 1550 to 631 nm [15]. We also use this technique to produce photons in arbitrary superpositions of these two widely separated frequencies, displaying high-contrast "Rabi oscillations" between the two energy states.

The second requirement is that the process must be coherent—if phase information is lost during the transduction process, the state of the qubit being transferred will not be preserved. Previous experiments have demonstrated that the photon statistics of the beam are preserved in the upconversion process [20]. Here we demonstrate the coherence of the process by preparing a weak 1550-nm pulse in a superposition of two time-bin states, upconverting to the visible, and measuring high-visibility interference fringes between the two time-bin states of the upconverted photon [21].

1.1 Upconversion Background

The non-linear field evolution equations for the process of frequency upconversion were given by Myers et al.[22],

$$\frac{dE_i}{d_z} = \frac{i\omega_i d_Q}{n_i c} E_o E_e^* \exp(i\Delta k_Q z) \tag{1.1}$$

$$\frac{dE_e}{d_z} = \frac{i\omega_e d_Q}{n_e c} E_o E_i^* \exp(i\Delta k_Q z) \tag{1.2}$$

$$\frac{dE_o}{d_z} = \frac{i\omega_o d_Q}{n_o c} E_i E_e \exp(-i\Delta k_Q z), \tag{1.3}$$

where ω_i, ω_e, and ω_o are the input, escort and output angular frequencies; n_i, n_e, and n_o are the indexes of refraction of the input, escort and output beams; d_Q is the effective non-linear coefficient; E_i, E_e, and E_o are the amplitudes of the input, escort, and output electric fields; z is the position in the crystal; and Δk_Q is the phase mismatch, given by

$$\Delta k_Q = 2\pi \left(\frac{n_o}{\lambda_o} - \frac{n_i}{\lambda_i} - \frac{n_e}{\lambda_e} \right). \tag{1.4}$$

However, in order for this to be a valid process we must satisfy conservation of energy such that $\omega_i + \omega_e = \omega_o$, or equivalently

$$\frac{1}{\lambda_o} - \frac{1}{\lambda_i} - \frac{1}{\lambda_e} = 0, \tag{1.5}$$

To simplify our analysis we make two approximations. The first is the non-depletion limit, which assumes that $E_e \gg E_i$ and $E_e \gg E_o$, and therefore equation 1.2 may be approximated by

$$\frac{dE_e}{d_z} \approx 0. \tag{1.6}$$

The second approximation is the phasematching approximation, which assumes that $\Delta k_Q \approx 0$. This is true when our three-wave mixing process conserves momentum. After these two approximations are made, we arrive at our reduced field evolution equations

$$\frac{dE_i}{d_z} = \frac{i\omega_i d_Q}{n_i c} E_o E_e^* \tag{1.7}$$

$$\frac{dE_o}{d_z} = \frac{i\omega_o d_Q}{n_o c} E_i E_e. \tag{1.8}$$

From these relations we calculate the quantum state evolution and the probability of upconversion $P_o(z)$:

$$P_o(z) = \sin^2 \left(\sqrt{\frac{\omega_i \omega_o d_Q^2 |E_e|^2}{n_i n_o c^2}} z \right), \tag{1.9}$$

By choosing an appropriate crystal length L such that $P_o(L) = 1$, one can in principle achieve near unit conversion efficiency. The efficiency in practice is limited by losses and how well one can match the spatial, spectral, and temporal modes of the interfering light fields.

We can achieve the non-depletion limit by simply choosing an escort beam which is much stronger than our input. Other work on high-efficiency upconversion has employed continuous pumping beams, using either a buildup cavity

[12] or non-linear crystals with waveguide structures [11, 21] to achieve the high intensities required. Our scheme instead relies on using bright escort *pulses* in a bulk, quasi-phased-matched Periodically Poled Lithium Niobate (PPLN) crystal, thus avoiding the insertion loss of waveguide structures and cavities, and leading to reduced background. However, achieving $\Delta k_Q = 0$ is somewhat more difficult. We notice that the form of Equations 1.5 and 1.4 are similar, except that Δk_Q depends on the three indices of refraction, n_i, n_e, and n_o. These two conserved quantities would be trivially equivalent if the nonlinear material were not dispersive. While the material is, in fact, dispersive, it is possible to compensate for the dispersion by using different polarizations of light and using the birefringence of the crystal to compensate for the dispersion; however, this limits us to the relatively smaller nonlinear coefficients of the $\chi^{(2)}$ nonlinear susceptibility tensor that couple orthogonal polarizations.

1.2 Periodic Poling

A better way to compensate for the dispersion is to use periodically poled materials, such as periodically poled lithium niobate (PPLN). These materials use periodic reversals in the ferroelectric domain. The direction of the domain determines the phase relationship between the input, escort, and output wavelengths (see section 2.2). Normally, dispersion causes a phase mismatch between the light generated at the beginning of the crystal, and the light generated at a later point inside the crystal. This phase mismatch increases linearly with the length of crystal. If, by controlling the direction of the domain, we can reverse the sign of the phase of the generated light, the dispersion is effectively negated. We call this quasi-phasematching; it differs from the above dynamics in two ways. First, we must amend our conservation of momentum relation to include the component contributed by the poling of the crystal.

$$\frac{\Delta k_Q}{2\pi} = \frac{n_o}{\lambda_o} - \frac{n_i}{\lambda_i} - \frac{n_e}{\lambda_e} - \frac{1}{\Lambda} = 0, \tag{1.10}$$

where Λ is the poling period of the crystal. The second modification is that we must use an effective d_Q which is reduced by a factor of $2/\pi$ from the unpoled case. This is due to averaging over all of the phases of upconverted light between 0 and π that are excited throughout the domain. Since we are free to make Λ equal whatever we like (within the limits of our poling technology), we will always be able to satisfy conservation of momentum.

The crystals are made by applying a photoresist mask to the crystal substrate; the crystal is then lithographed with ultraviolet light in the pattern of the desired periodic domains. A liquid electrode is poured over the crystal and a voltage is applied between the top periodic electrode and a conductor on the bottom of the crystal. The strong applied electric field causes the ferroelectric domain of exposed regions of the crystal to realign with the field. This process

is similar to realigning the direction of magnetic domain in a ferrous material using a strong magnetic field. As with ferromagnetic materials, the domains can be annealed out by excessive heating, and so one must be careful not to heat our crystal too much during temperature tuning. We purchased crystals with poling periods of 11.4 μm from HC Photonics.

1.3 Experiments on Upconversion

To explore the potential for using frequency upconversion in quantum information applications, we first designed a series of numerical models which allow us to easily evaluate all of the significant parameters, including input and escort wavelength; escort power; spatial and temporal modes; crystal poling period and temperature; and crystal dispersion, which we describe in Chapter 2. Using these models we can simulate various upconversion configurations and predict the tolerances that will be required to achieve the high efficiency levels necessary for our applications.

In Chapter 3, we describe the construction of a detection system for infrared (IR) single photons that upconverts them to the visible and uses a silicon avalanche photodiode (APD) to detect the upconverted photon. Normally, InGaAs APDs are used to detect photons in the 1550-nm (C-band) range; however, these diodes have very poor efficiency and high dark counts. By leveraging the superior performance characteristics of silicon single-photon detectors at visible wavelengths with frequency upconversion, we are able to achieve a 99%-efficient conversion process, resulting in a net 56%-efficient detection of single photons at 1550 nm by upconverting them to 631 nm with a 1064-nm escort laser. This is vastly superior to the typically 10%-efficient InGaAs detectors and exceeds the threshold of 50%-efficient detection required, e.g., for cluster state quantum computation [23].

Once we were able to achieve near-unit conversion efficiency, we explored creating single-photons in superpositions of the input and output wavelengths, as describe in Chapter 5. By adjusting the power of the escort, we were able to precisely control the amount of conversion from the lower frequency to the higher. This process bears a striking resemblance to Rabi oscillations in an atom; however, instead of transforming between two electron energy levels of an atom, we are transforming between two frequency states of a photon. We attempted a range of oscillations from 0 to 3π, and observed several Rabi fringes in the frequency state of a photon.

We verified the coherence of the upconversion process in Chapter 4 by placing an upconversion system in between two overlapping, unbalanced Michelson interferometers. The first interferometer created a photon in a superposition of two time-bin states, which were then upconverted independently. The second interferometer measured the phase relationship between the two time-bin components of the upconverted photon. We observed a 95% visibility in the

coherence of the upconverted photons, qualifing the system for use in quantum information systems where the coherence of the qubit must be preserved.

Finally, as described in Chapter 6, we constructed a high-speed coherent switching system based on upconversion. After verifying the Rabi-like and coherent nature of the system, we noted that a π Rabi pulse leaves the system in the original state with the opposite sign (a π phase shift). We used this π-phase-modulation system together with a variety of interferometers, and were able to demonstrate high-speed, transparent, coherent, switching. We proposed extensions to this scheme which may achieve bias-free and frequency-multiplexed switching operation.

The upconversion techniques we have explored here hold significant promise for quantum information applications. Potential future research efforts include waveguide based upconversion, which significantly lowers the escort power requirements by tightly confining modes in waveguides to achieve the necessary fields for efficient conversion. Applications such as quantum repeaters and upconversion-based quantum key distribution systems over fiber optic networks would benefit from the enhanced detection at 1550 nm. Additionally, we propose some new applications which require experimental implementation, e.g., atomic simulations (Section 5.5) and frequency-multiplex switching (Section 6.5).

2 Numerical Modeling

2.1 Simulation Introduction

We intend to use frequency upconversion for several high-precision experiments. However, before we can commence with these experiments, we need to know the precise character of our system and be able to predict the tolerances for our apparatus. To model the upconversion system, we constructed a numerical simulation–written in scheme–of the three-wave mixing process (see Appendix A). The model numerically integrates the coupled field-evolution equations (Equations 1.1-1.3) and allows exploring the parameter space of beam wavelengths, beam intensities, crystal poling period, length, temperature, and spatial and temporal modes. Using this model we are able to accurately predict the performance of our system from our actual experimental parameters.

2.2 Field Evolution Approximations

Our experiments with high-efficiency upconversion use periodically poled nonlinear materials, and so we first examine the effects of poling in a material. To allow thee-vibrational modes of the electric field to couple strongly, we must have an interaction that satisfies conservation of energy and momentum. The momentum of a photon inside a crystal depends on its index of refraction, therefore, simultaneously satisfying these two conserved quantities would normally be impossible because of dispersion in the material. Previous types of thee-wave mixing in $\chi^{(2)}$ materials used either type-I or type-II phasematching, whereby birefringence is used to compensate for dispersion; however, this forces the use of the smaller nonlinear coupling coefficients associated with coupling modes of perpendicular polarization. The technique of periodic poling allows use of the relatively large nonlinear coefficient that couples the extraordinary polarized modes together, by compensating for dispersion with periodic changes in the ferroelectric domain of the nonlinear crystal. This modulation in the ferroelectric domain is seen as a fourth wave in the process; it contributes a small amount to momentum conservation, but does not affect the energy conservation relation.

A simpler way to view the effect of poling on the nonlinear interaction is in terms of phase mismatch. Given the phases of the input and escort beams, we calculate the phase of the induced output field. However, because of disper-

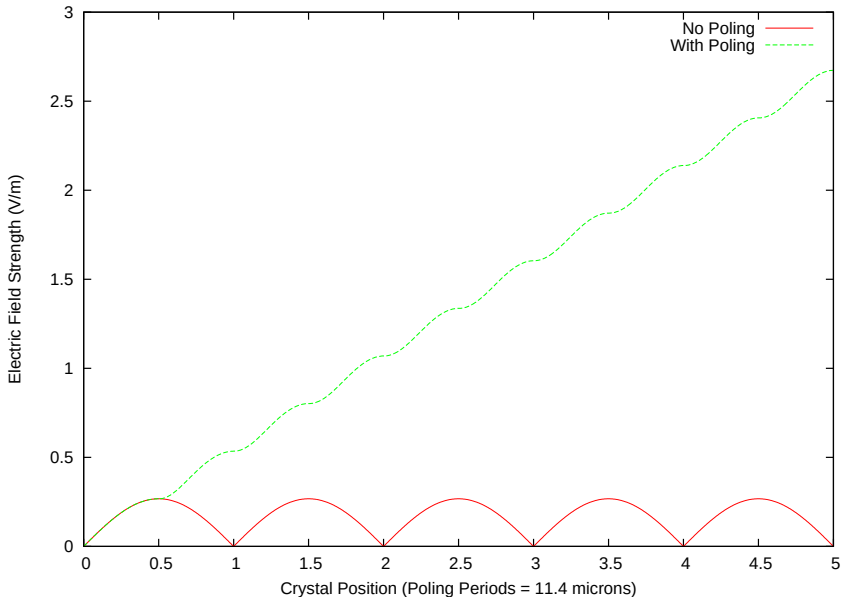

Figure 2.1: Electric field vs. position in the crystal for the poled and non-poled cases.

sion, the generated phase at one point in the crystal will be different than the generated phase at a different point in the crystal. When we sum up all of the excited modes over a long length of crystal, they all contribute equally, and so they tend to cancel out. In a periodically poled quasi-phasematching scenario, we invert the ferroelectric domain using a lithographic mask and strong electric fields at every point in the crystal where the difference between the phase excited at that point and phase excited at the beginning of the crystal equals π. The domain reversal effectively inverts the relationship between the phases of the unconverted signal and the escort and the phase of the upconverted light. Over the length of the crystal (typically thousands of domains) only phases between 0 and π are excited, rather than 0 and 2π, and so energy accumulates in the output field.

Figure 2.1 models the evolution of the output electric field inside of a crystal for the poled and non-poled cases. When there is no poling, and no means of compensating for dispersion, we find that a small amount of light is upconverted and then immediately downconverted back to zero. We repeat these tiny up and downconversion processes without accruing any significant strength in the output field. When the domain is inverted (every half period), some light is upconverted, and then just as what has been gained is about to downconvert, the domain is inverted and a little more light is upconverted.

Now that we know that periodic poling can upconvert light, even in the presence of dispersion, we would like to know if the relationship can be made simpler. The field evolution in Figure 2.1 was calculated using Equations 1.1-1.3 under the conditions that $\Delta k_Q \neq 0$ (since Equation 1.4 does not have a term

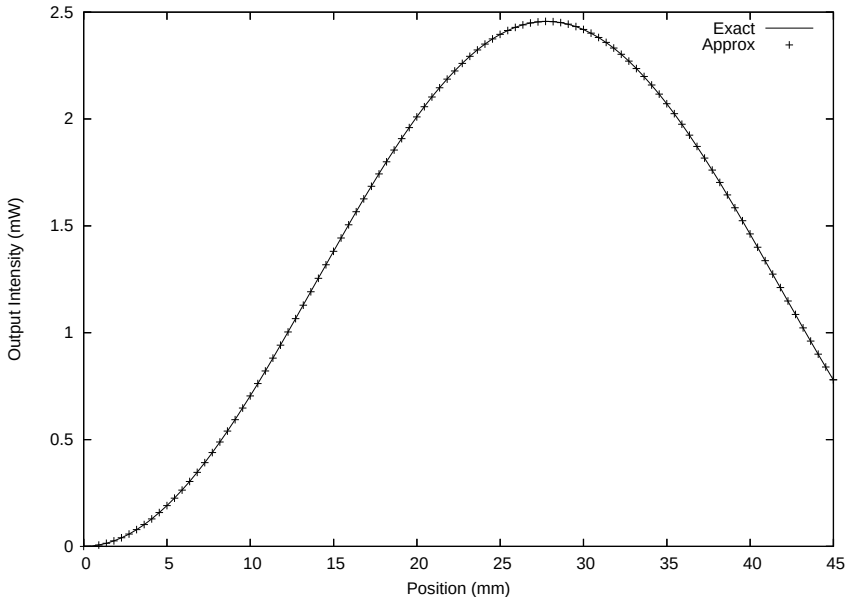

Figure 2.2: Output light predicted for 1-mW input power, 10-kW escort power, using exact numerical model and numerical model with non-depletion and quasi-phasematched approximations. The final output of the approximated model is 0.2% higher than the exact model.

representing the poling), and that $d_Q = \pm d_{33}$, depending on the position inside the crystal. The requirement to reverse the field is computationally expensive, since it requires integration on a granularity that is small compared to the poling domain size. By making the phasematching approximation ($\Delta k_Q \approx 0$; see Section 1.1) we can account for the effect of the domain structure by using the full form for Δk_Q (Equation 1.10), and by setting $d_Q = d_{33} 2/\pi$. The factor of $2/\pi$ is derived from averaging all of the unit vectors with angles from 0 to π during quasi-phasematching. We also note that the conversion process has very little effect on the escort beam, as long as the input is much weaker than the escort. By approximating $dE_e/dz \approx 0$ (the non-depletion approximation), we can reduce Equations 1.1-1.3 to Equations 1.7 and 1.8. By making these two approximations we obtain a set of two coupled, position-independent equations instead of three coupled, position-dependent equations, which should be more efficient to compute, provided the results are accurate.

Figure 2.2 shows the output power obtained by converting a 1-mm 1-mW Gaussian beam at 1550 nm with a 10-kW escort beam as it propagates through a 4.5-cm PPLN crystal. We calculate this scenario two different ways: a) modeled using direct periodic poling of a three-wave mixing process; b) modeled by making the non-depletion approximation and the quasi-phasematching approximation. The two graphs look very similar and the final predictions of the approximated model are accurate to within 0.2%. Therefore, we conclude that these approximations are valid to a level of precision sufficient for our purposes.

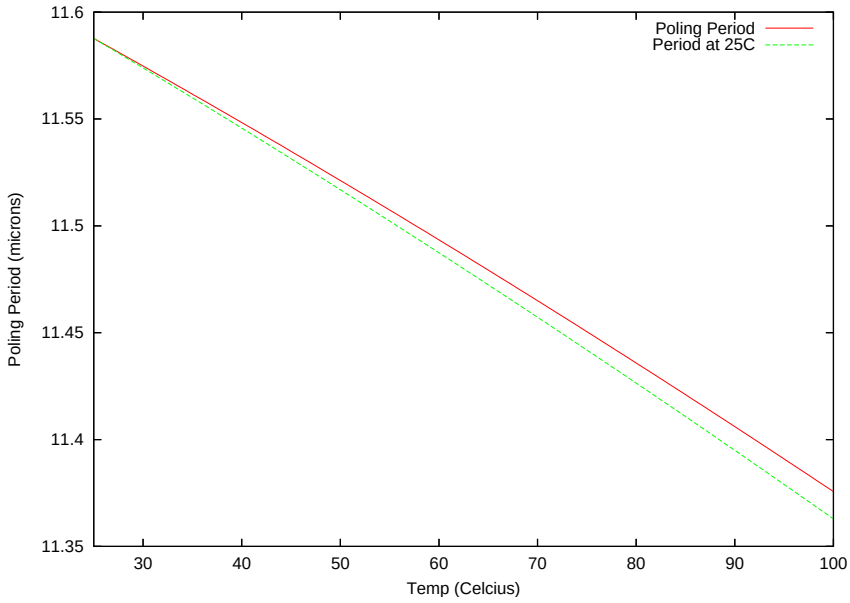

Figure 2.3: Calculated phasematching crystal poling period at operating temperature (solid) and at 25 °C (dashed) versus a given operating temperature. The graphs are sufficiently similar, so we can safely ignore the effects of thermal expansion when designing our system.

2.3 Phasematching

For an upconversion experiment to perform well, two major criteria need to be satisfied: phasematching and spatial mode matching. Spatial modes are generally relatively easy to match (though see Section 4.2); however, phasematching requires having the three wavelengths, the poling period, and the crystal temperature all in alignment. Coordinating the phasematching temperature and poling period simultaneously has the potential to be difficult, since the crystal's poling period at room temperature is different that its period when heated to the desired phasematching temperature due to thermal expansion. We investigate the effect of thermal expansion in Figure 2.3. We graph the poling period a crystal must have when at operating and room temperatures to phasematch a 1064-nm escort with a 1550-nm input laser versus operating temperature. We find that the the temperature dependence of the indices of refraction is much larger than the geometric thermal expansion coefficient, and so although the poling period is somewhat affected by thermal expansion, it is not necessary to account for thermal expansion when manufacturing a poled crystal. We can easily compensate for the error in poling period due to thermal expansion by temperature-tuning a few degrees.

Once we have our crystal, we would like to know how useful it will be for converting various wavelengths. Given a specific poling period and temperature, Figure 2.4 plots the escort wavelength required to upconvert various input wavelengths. We have plotted this for three models of dispersion. The "zero lo-

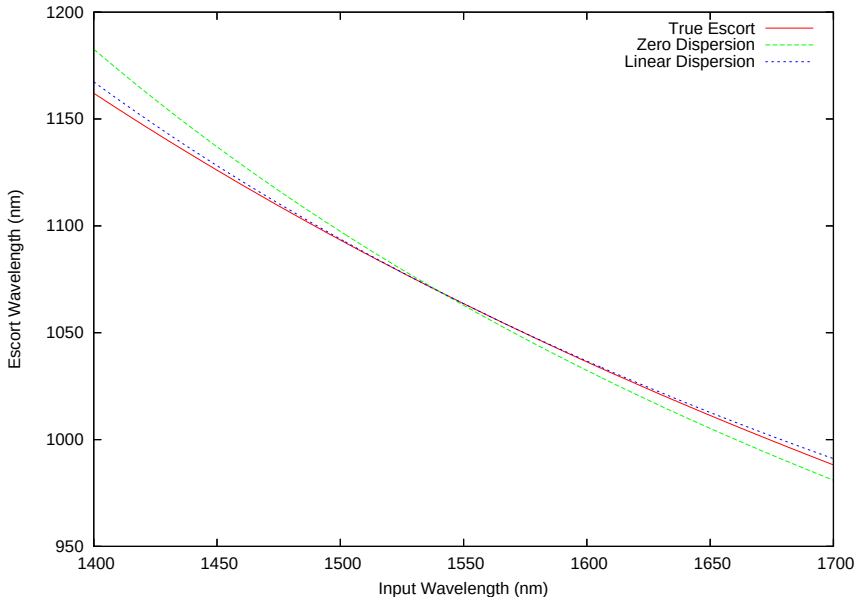

Figure 2.4: Phasematched escort wavelength versus input wavelength for the different models of dispersion: zero local dispersion, linear dispersion, and the full Sellmeier dispersion equation. The poling period and temperature are held constant at 11.4 μm and 94.8 °C, respectively.

cal dispersion" model assumes that the index is constant near the input, escort, and output wavelengths. The "linear dispersion" model assumes that the index varies linearly with wavelength near the three relevant wavelengths. Lastly, the "true" model is calculated based on the complete temperature-dependent Sellmeier equation. We graph the three models together to see how accurate they are in determining the required escort. While we may numerically calculate the escort using the true model, the zero and linear models are analytically simpler and can provide useful insight into more complex phasematching situations (see Section 5.5).

In addition to versatility in escort wavelength, we would also like know how versatile a crystal with a given poling period might be in converting various wavelengths when we cannot tune the escort. This is a more accurate representation of our experimental setup, since our escort laser is a Nd:YAG pump, which is fixed at 1064 nm. Instead of tuning the escort wavelength to phasematch a given input wavelength, we can use temperature tuning. Figure 2.5 plots the temperature required for a range of input wavelengths. The ovens and temperature controllers we use have a useful range of about 40-130 C, which give a useful input frequency band of ∼30 nm. The two near-IR input sources we have operate at 1550 nm and 1544 nm, corresponding to phasematching temperatures of 92.1 °C and 73.3 °C, respectively. The ovens themselves are capable of operating at temperatures higher than 130 °C; however, we must operate the crystal below those temperatures in order to prevent the poled domain

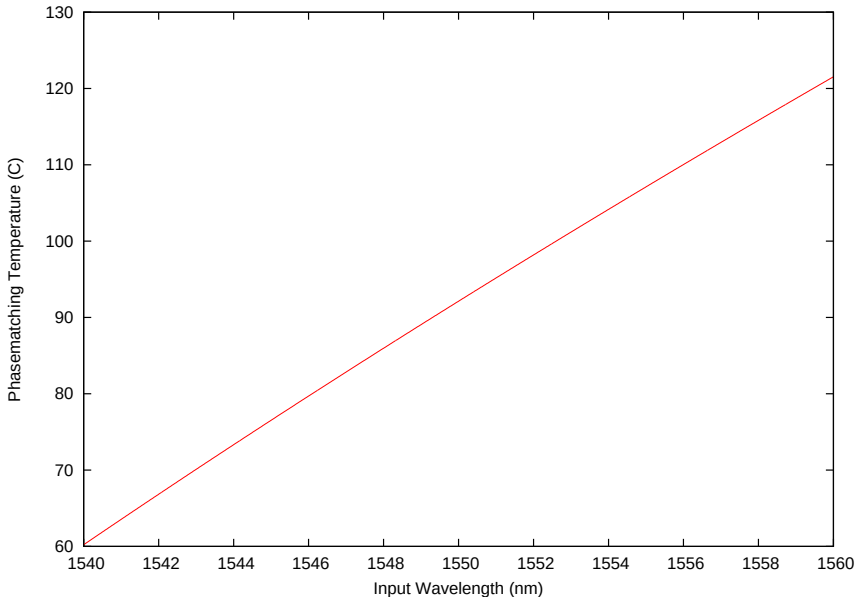

Figure 2.5: Phasematching temperature for a range of wavelengths. The escort wavelength is held constant at 1064 nm and the poling period is assumed to be 11.4 μm.

structure from annealing out.

2.4 High-Efficiency Tolerances

Once we have established what the quasi-phasematching parameters should be, and how flexible they are, we need to determine what the tolerances of those values are. In Figure 2.6 we plot the conversion efficiency as we scan the poling period through the phasematched 11.4 μm. We notice that the width of the curve is only a few nm. We can use temperature tuning to correct the errors in the poling period by up to 100 nm (Figure 2.3); however, we must still require a high level of uniformity in the poling period. For example, a 5-nm chirp in the poling period would effectively cut the usable crystal length in half. A 5-nm jitter in the poling period would render the crystal unusable. In order to achieve very high conversion efficiencies, we require that the poling be highly consistent.

Figure 2.7 shows us the temperature tuning curve. The peak is a few degrees wide; however, we wish to operate in the regime where 99% of our light is converted, so we need temperature stability on the order of 0.2 °C. This graph looks very similar to a sinc^2 function, but it is not, since the ratio of the first peak to the central peak is too large. The actual efficiency η is given by

$$\eta = \frac{\omega_i \omega_o d_Q^2 |E_e|^2 z^2}{n_i n_o c^2} \mathrm{sinc}^2 \left(\sqrt{\frac{\omega_i \omega_o d_Q^2 |E_e|^2}{n_i n_o c^2} + \frac{\Delta k_Q^2}{4}} z \right), \tag{2.1}$$

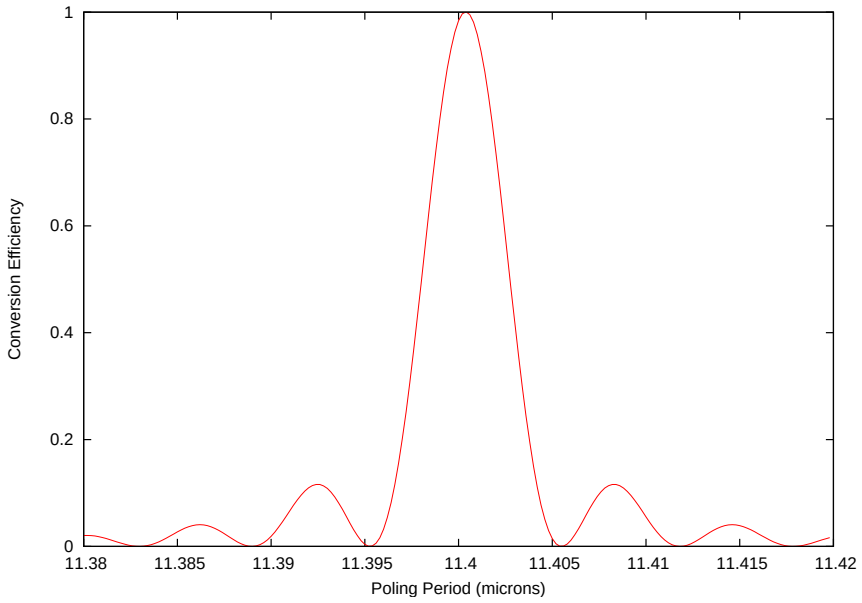

Figure 2.6: Predicted conversion efficiency for fixed wavelengths over a range of poling periods. Input and escort wavelengths are 1550 and 1064 nm, crystal length is 22 mm, temperature was 92 °C, and the escort power was 1 kW with a 177-μm spot size.

where the temperature dependence is expressed in the temperature dependence of n_i, n_o and Δk_Q (see Section 1.2). We must still take note of its shape, however, since when we perform temperature tuning (Section 3.6) we must be careful not to optimize toward one of the local maxima side peaks, and instead thoroughly scan the temperature to identify the central peak.

A similar sinc^2-like function appears when we plot the conversion efficiency for a range of input wavelengths. Our tunable 1544-nm source has a range of 2 nm, which is sufficient to sweep though the central peak and demonstrate wavelength multiplexing capabilities of the upconversion system (see Figure 6.4). The conversion efficiency versus input wavelength curve, however, determines the bandwidth of an upconversion channel. We will not be able to upconvert a signal of wider bandwidth than this tuning peak with a monochromatic escort. The widths of these phasematching tuning curves vary with the length of the crystal. As the crystal goes longer, small perturbations in the phasematching conditions accumulate, causing the phasematching requirements for high efficiency to become more strict and the widths of the tuning curves to decrease. In Figures 2.9 and 2.10 we plot the full width at half maximum (FWHM) and full width at 90% maximum (FW90%M) of the tuning curves for temperature and input wavelength, respectively. For our precision experiments, we endevoured to keep the tolerances below the FW90%M level.

In addition to the direct phasematching parameters, we would also like to examine the effects of temporal modes on phasematching. We will use a pulsed

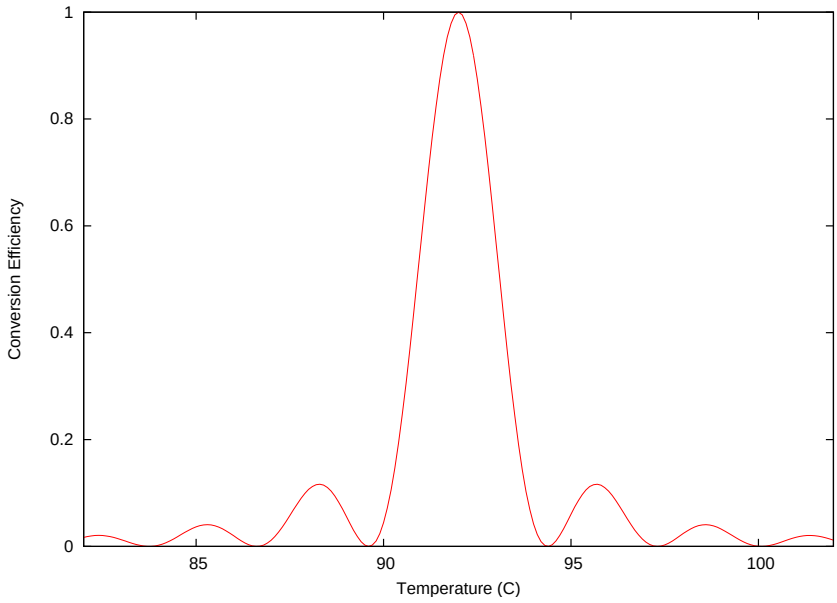

Figure 2.7: Predicted conversion efficiency over a range of temperatures.

configuration to achieve the high escort intensities required for efficient conversion, and therefore must examine the relationship between escort and input pulse lengths. In Figure 2.11, we plot the predicted conversion efficiency for various 1550-nm input pulse widths using a 600-ps 1064-nm escort beam. For very long input pulses, most of the input pulse lies outside the escort pulse, and so the conversion is suppressed, since only the input light which is very near the peak of the escort is efficiently converted. As we decrease the input pulse length, the total efficiency rises; however, this also has the effect of broadening the input pulse bandwidth, since the input pulse has a minimum bandwidth determined by the Fourier transform limit of the temporal width. We know from Figure 2.8 that only a narrow band of wavelengths will convert for a given crystal and monochromatic escort. As the concomitant spread in wavelengths from shortening the input pulse becomes broader than the width of the spectral tuning curve, the total conversion efficiency decreases. We find an optimum input pulse with of 140 ps, yielding a predicted maximum conversion efficiency of 99.7%.

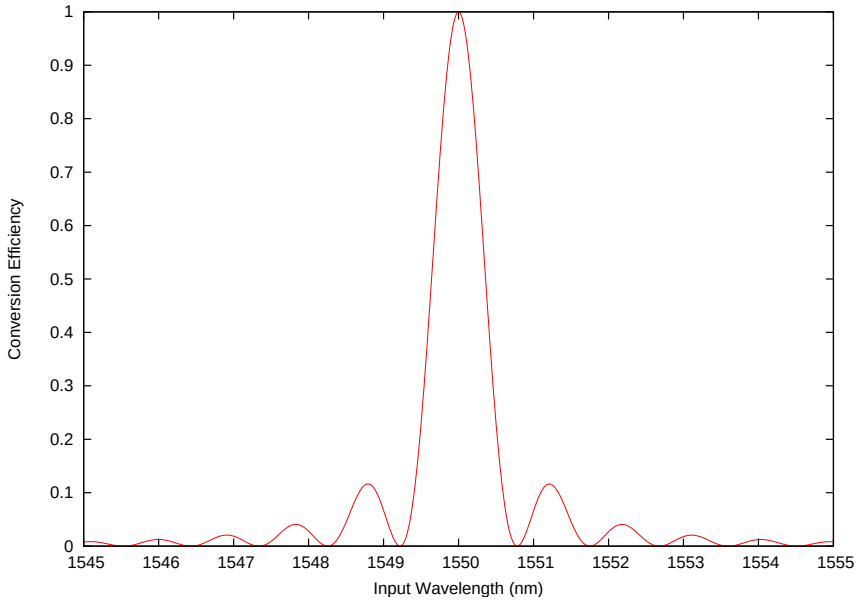

Figure 2.8: Predicted conversion efficiency over a range of input wavelengths.

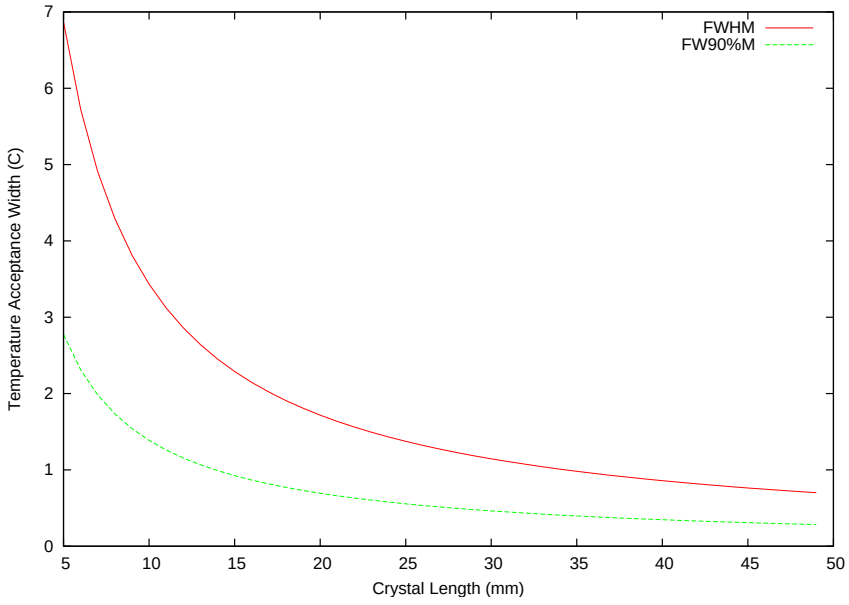

Figure 2.9: Width of the temperature tuning curve (Figure 2.7) for various crystal lengths.

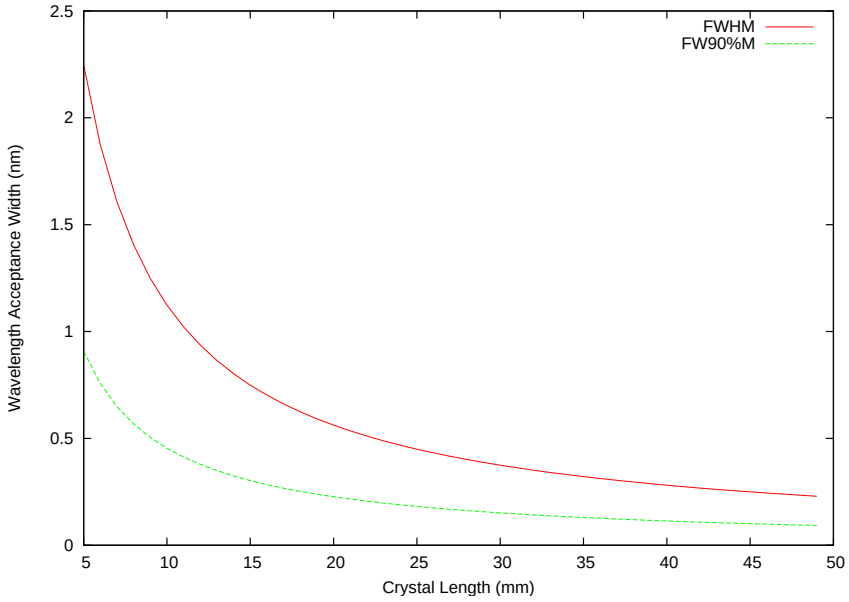

Figure 2.10: Width of the input wavelength tuning curve (Figure 2.8) for various crystal lengths.

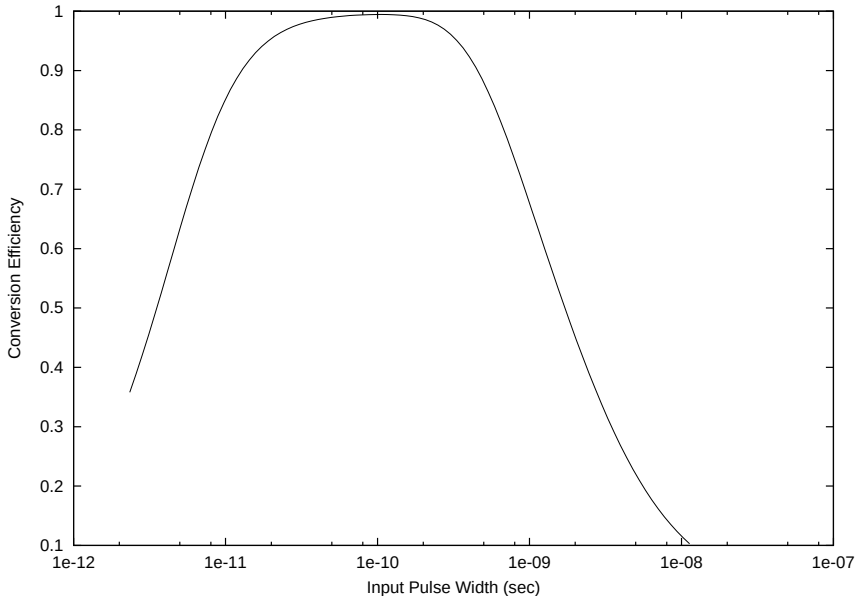

Figure 2.11: Predicted conversion efficiency vs. 1550-nm input pulse width. 1550-nm light is upconverted using a 1064-nm 600-ps escort pulse. If the input pulse is too long, the temporal overlap is reduced, lowering efficiency. If the pulse is too short, the spectral width of the pulse becomes very wide, inhibiting phasematching and reducing efficiency.

3 Detection

3.1 Detection Introduction

Efficient single-photon detectors are an important resource for many applications. In quantum information, schemes such as quantum key distribution (QKD) have bit-rates directly dependent on the efficiency of the receiver's detector. Since the telecommunications infrastructure is optimized for near-IR signals (e.g., 1550 nm) single-photon detectors sensitive to these wavelengths would benefit the performance of these systems. Unfortunately, the most common detectors sensitive to 1550-nm photons are based on indium gallium arsenide (InGaAs) avalanche photodiodes (APD). These have performance characteristics vastly inferior to their silicon counterparts. Their quantum efficiencies are around 10% [24] compared to greater than 70% for silicon. The InGaAs detectors also have much higher dark counts (10^4/s) and afterpulsing probabilities than silicon. Finally, in order to combat the high dark couts, the InGaAs diodes must be cooled and are more expensive than silicon, further limiting their usefulness. The only positive characteristic that InGaAs diodes have is that they are sensitive to C-band 1550-nm photons, a range that silicon detectors are blind to. Other detectors such as those based on superconducting transitions offer the promise of enhanced detection of 1550-nm photons, but they are still in the early phases of development and the liquid helium temperatures they require may make them prohibitively expensive.

Classical long-haul telecommunications, where the signal light is attenuated over vast distances ($>$ 1 Mm) in fiber, causing the signal power to fall to the single-photon level, would also benefit from IR single-photon detectors. Linear optics quantum computation [25], such as cluster-state computation [23], have high detection efficiency thresholds to be viable schemes of quantum computation. In addition, detection of single atoms and molecules with transitions in the IR range require detection of fluorescence photons. IR single-photon detectors could also enhance IR astronomy by allowing imaging of distant objects so faint that only a handful of photons reach the telescope.

With the exception of wavelength sensitivity, silicon APDs are superior to InGaAs APDs in every capacity. We use frequency upconversion to shift IR photons into the visible range where they can be detected by a silicon detector. As long as the conversion process has sufficiently high efficiency and low noise, we are able to leverage the high performance characteristics of the silicon diodes

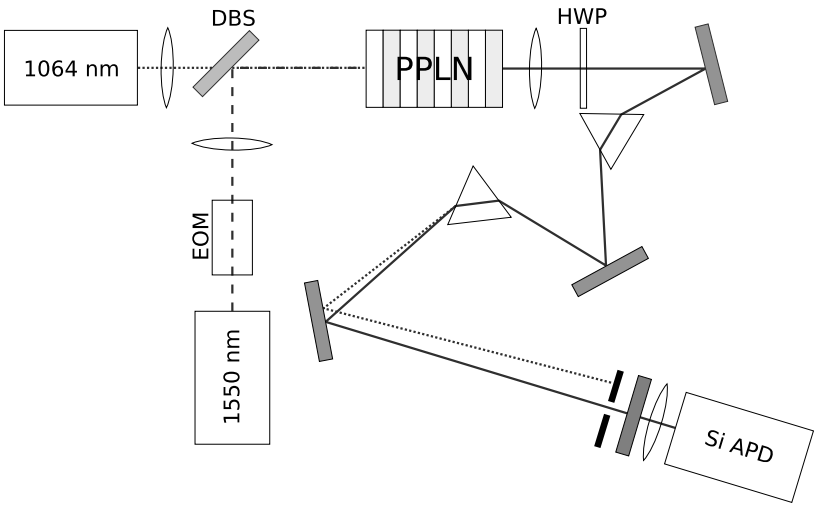

Figure 3.1: High efficiency upconversion experiment. A weak 1550-nm pulse is combined on a dichroic beam splitter (DBS) with a bright 1064-nm escort pulse and focused into a non-linear crystal (PPLN). The 631-nm upconverted pulse is then filtered through dispersion prisms and an interference filter, and finally detected by a silicon Avalanche Photodiode (APD).

to achieve higher efficiency, lower noise detection of IR photons at 1550 nm.

3.2 Upconversion Detector Overview

As shown in Fig. 3.1, our 1550-nm photons are combined on a dichroic beam splitter with very bright escort pulses from a passively Q-switched Nd:YAG laser that produces 600-ps wide pulses (Figure 3.2) at 1064 nm. We optically delay the escort pulses (Section 3.3) to allow time for input pulse generation, before a variable attenuator (Section 3.4) adjusts the intensity of the escort pulse. In Section 3.6 we discuss how the escort is then focused to a spot at the midpoint of a PPLN crystal while the input beam is focused inside the crystal onto the center of the escort beam spot.

Since the probability of upconversion $P_o(z)$ depends on the intensity of the escort ($|E_e|^2$), and our pulsed escort necessarily has a time-varying intensity, we make the input pulse much shorter than the escort pulse so that the input photon experiences only the (relatively constant) peak intensity of the escort. However, the 1550-nm pulse duration cannot be too short, or the concomitant spread in frequencies will fall outside the phase-matching bandwidth for efficient upconversion. The 1550-nm light is produced from a telecom diode laser and passed through a pair of waveguide electrooptic intensity modulators (EOM), creating pulses that are 200 ps wide (Section 3.5). The EOMs are triggered by the escort laser, thereby synchronizing the 1550-nm pulse to the escort. A calibrated attenuator reduces the mean number of photons per pulse to < 1,

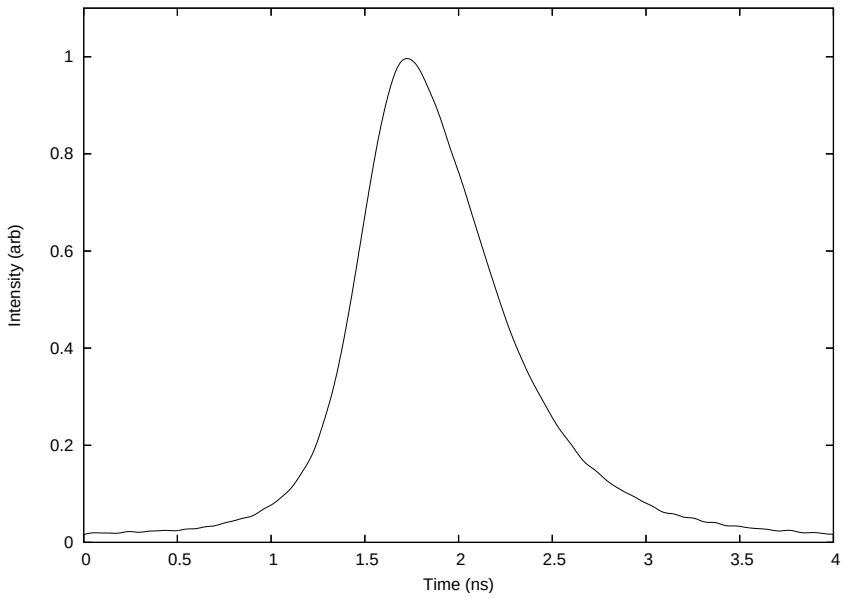

Figure 3.2: Oscilloscope trace of escort laser. The JDS Uniphase DNP-150010-000 DualChip NanoPulse Laser generates ∼600-ps pulses at 1064 nm with a repetition rate of 44.1 kHz. The trace was taken using an EOT InGaAs PIN photodiode (EOT model ET-3500F) connected to an HP Agilent 81000FA Signal Analyzer Mainframe.

thus closely approximating a superposition of a single-photon Fock state and the vacuum[1]. We upconverted 1550-nm light at a wide range of input powers, measured the power of output light, and found it to be highly linear (Figure 3.3). This result implies that the conversion process simply maps the state of the light from the lower frequency to the higher one. Upconverting a coherent state yields a coherent state while upconverting a Fock state yields a Fock state.

3.3 Escort Delay

Our escort laser is a pulsed, passively Q-switched, 500-mW, 44.1-kHz Nd:YAG laser from JDS Uniphase (DNP-150010-000 DualChip NanoPulse Laser). The passively Q-switched mode of operation has the advantage of producing the high peak intensities necessary for efficient conversion, but it makes the pulse timing somewhat erratic. We require that the escort and input pulses arrive simultaneously at the upconversion crystal, to an degree small compared to the 600-ps pulsewidth of the escort. The escort laser pulse-to-pulse jitter is a few

[1] under the assumption that our laser outputs a coherent state. However, see, e.g., Pegg and Jeffers[26] and references therein

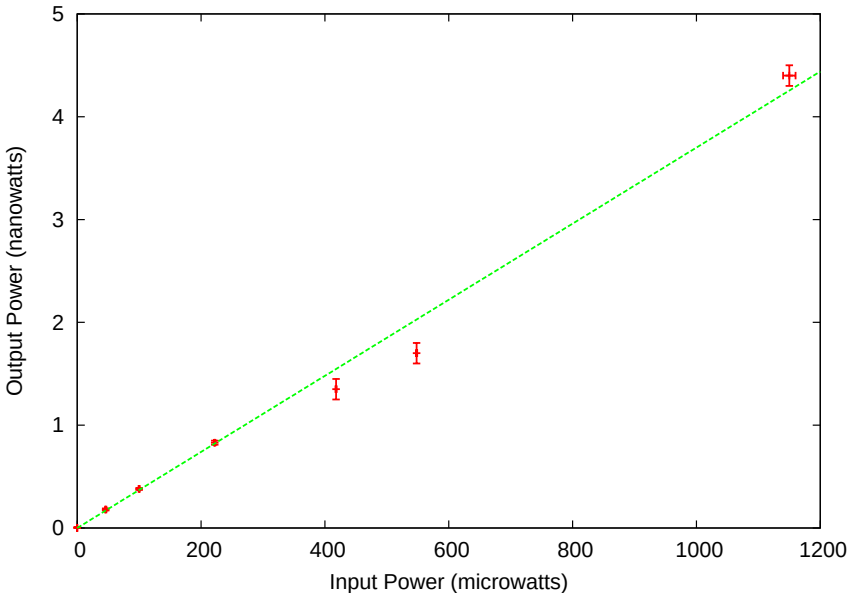

Figure 3.3: Power of converted light is plotted against input power. The overall conversion efficiency is low due to the low duty cycle of the escort laser (600-ps pulses at 7.2 kHz), since the input beam was CW, the escort was pulsed, and only the input light coincident with an escort pulse. The data show the conversion process is highly linear over several orders of magnitude. The lowest-power point on the graph was measured using a silicon APD single-photon counter, while the other points were measured using a Newport 818-SL Power Meter.

microseconds[2], which prohibits us from using the previous pulse to coordinate the timing of the input photon with the escort pulse. Instead, we detect when an escort pulse is generated by using the inherent crosstalk of a polarizing beam-splitter to pick off a small amount of the escort beam as soon as it exits the source. We detect this signal with an ultra-fast photodiode (AEPX-65), which has a jitter below 8 ps, and use the electrical signal to trigger the creation of a 1550-nm input photon (by driving the EOMs in the 1550-nm beam).

From the time we generate an electrical pulse synchronized to the escort, it takes ∼100 ns to process the signal and create the input 1550-nm pulse. In order for the two pulses to arrive at the crystal simultaneously, we must delay the escort pulse. We direct the escort beam into a Harriot cell (not shown in Figure 3.1) constructed of two spherical curved mirrors. The mirrors are 2 inches in diameter, have 5-mm holes 20-mm from the center, and a radius of curvature of 1 m. They are placed ∼95 cm apart in a just-inside-confocal arrangement.

[2]It my be possible to force the passively Q-switched Nd:YAG laser into an actively switched mode by feeding a pulsed diode laser into the output coupler of the Nd:YAG laser. If the diode laser pulses at a frequency slightly higher than the natural frequency of the escort laser, and the pulse has the proper energy and wavelength to transmit through the output coupler and be absorbed in the Cr:YAG saturable absorber that regulates the passive Q-switching, the absorber bleaching and consequently the Nd:YAG pulse will be synchronized to the diode laser pulse. This "trigger-laser" configuration could potentially reduce the escort jitter sufficiently to eliminate the need for the escort delay line. See Basiev et al. [27, 28]

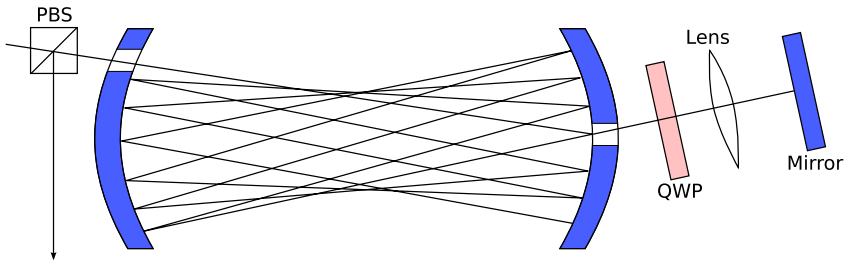

Figure 3.4: Diagram of a Harriot cell delay line with "time reversal" mirror. A horizontally polarized beam enters though a 5-mm hole in a curved mirror, bounces several times between the two curved mirrors, and exits a hole in the opposite mirror. It is then partially rotated by a quarter waveplate (QWP), focused with a lens, and reflected at the focal point by the mirror. It then retraces its path backwards, rotating to vertical polarization, and again bouncing several times on the curved mirrors. Finally it reflects off of the polarizing beamsplitter (PBS), having been delayed some ∼200 ns.

The beam enters the cell through the hole in one of the mirrors and bounces between the two mirrors 20 times in a circular spot pattern before exiting via the hole on the opposite mirror (Figure 3.4).

The circular mirrors refocus the beam on each pass so that the spot size has not significantly changed even though the total path is much longer than the Rayleigh length of the beam. Nevertheless, the curvature of the mirrors does introduce a slight aberration which would limit the spot size of the beam were we to immediately focus it into the crystal. Instead, we pass the beam through a lens and retroreflect it off of a mirror in the focal plane of the lens, effectively time reversing the beam. A quarter waveplate is placed between the mirror and the lens so that the polarization is rotated 90°. The beam then retraces its original path in reverse so that the distortion so far accumulated is reversed. The beam finally exits the cell out of the same hole it entered. The polarizing beam splitter used to pick off the timing signal, which initially transmitted nearly all the beam, now reflects the beam as its polarization has been rotated by the quarter waveplate. The resulting escort pulse has been delayed ∼200 ns and is in a low-distortion Gaussian mode.

3.4 Escort Attenuation

Maximizing the amount of input light that is upconverted requires precise control of the peak intensity of the escort. If too little 1064-nm light is applied, some of the input light is left in the 1550-nm state; if too much is applied, some of the upconverted light is downconverted back to the 1550-nm state. The laser emits high intensity pulses (∼20 kW peak power) and so we only require a means to attenuate it to the proper level; however, we must be able to do so without disturbing the spatial mode so that the beam may be aligned at one

level and operated at another. The beam profiler (Gentec EO BeamScope-P9) used to do the alignment is quite sensitive, and the amount of light required for peak upconversion is much greater than the saturation level of the profiler head; therefore, we attenuate it an additional factor of 100 below I_0, the intensity required for peak conversion, to perform the alignment, and then reduce the attenuation so the escort is set to I_0. The best method we found that allows for both the required dynamic range as well as the spatial mode stability is to use a Newport model 925B Compensated Attenuator. This attenuator is constructed from two wedged glass filters. The optical density of each wedge varies linearly and so when they are positioned with their gradients in opposite directions they produce a filter of constant optical density. The net transparency is controlled by sliding the two wedges along each other in the direction of the gradient. The walkoff associated with passing through the two wedges is minimized by allowing the beam to be normal to the front and back surfaces of the two wedges, preserving the spatial mode as it passes through. The optical path length does change slightly as the two wedges are translated, which affects the position of the beam waist, however, if we defocus and collimate the beam as it passes through the filter so that the difference in optical pathlength is small compared to the Rayleigh range of the beam, the perturbation of the beam focus will be insignificant.

We experimented with other methods of attenuating the beam such as placing two polarizers in the path of the beam and rotating the upstream one. This technique had the advantage of repeatability since the rotation angle of the polarizer could be easily measured. However, it suffered from small dynamic range. The attenuation was too sensitive when the polarizers were close to orthogonal, and so the effective dynamic range was only about 2 orders of magnitude. Second, if the polarizer was wedged, or if the axis of rotation was not normal to the surface of the polarizer, rotating it would adversely affect the spatial mode. And finally, the polarizers we used (OptoSigma model 069-1105 dichroic polarizer) have a low damage threshold and are prone to melting when exposed to the high intensity of the 500-mW Nd:YAG escort laser.

3.5 Input Pulse Generation

Ideally we would be able to emit perfect single-photon Fock-state pulses on demand; however, this is not currently possible. Instead we use attenuated coherent states to create pulses which have mean photon numbers less than 1. An attenuated coherent pulse with a mean photon number of 0.2 is well approximated by a superposition of the single-photon Fock state and the vacuum state. The states are created in synchronization with the escort pulse by detecting the escort trigger pulse with a programmable delay generator (Stanford Research Systems DG-535 Delay Generator) and using its output to drive the 1550-nm EOMs. We can change the variable delay produced by this component to easily

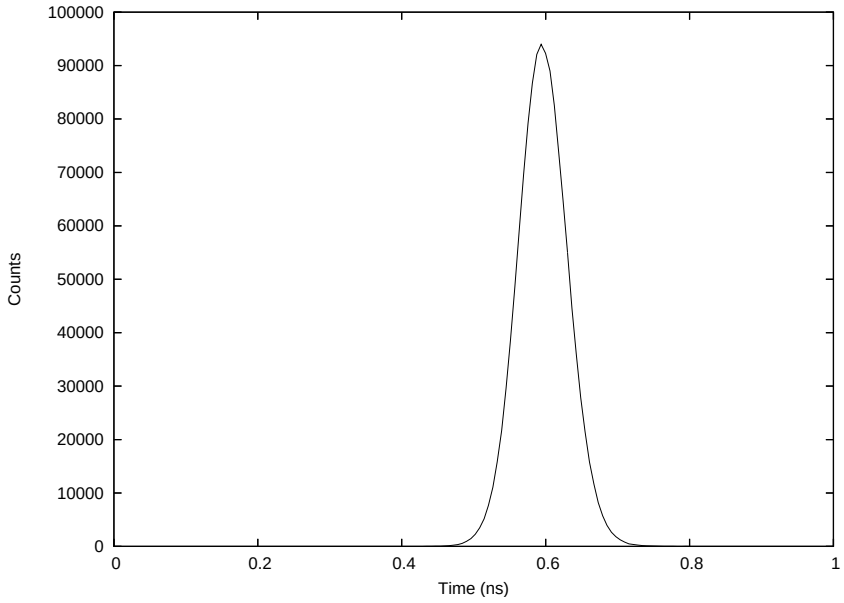

Figure 3.5: Timing jitter of the input pulse driver system is measured at 82 ps. We used the escort laser to create trigger pulses on two identical AEPX-65 fast photodiodes. The signal from the first diode is used to trigger the input pulse driver system, which is then used to start a time-to-amplitude converter (TAC), while the second diode signal–which is optically delayed from the first using the Harriot cell delay line (Figure 3.4)–is used to stop the TAC. We count the TAC pulses on a multichannel analyzer (MCA) and from the resulting distribution obtain the input pulse jitter.

shift the relative delay of the input and escort pulses to maximize overlap in the crystal. The delay generator outputs two pulses with adjustable delays. The first pulse triggers an Avtech picosecond pulse generator (Avtech AVP-2S-C-P-UILB Pulse Generator), which in turn creates a short, ∼200-ps electrical pulse that drives an electrooptic modulator (EO Space AX-0K2-20-PFU-PFUP-PD-R3 EOM). The second signal from the delay generator drives a second EOM (JDS Uniphase X5 EOM and JDS Uniphase H301 modulator driver). Light from a CW 1550-nm 20-mW fiber laser diode (Agilent 81663A lightwave transmitter and Agilent 8163A mainframe) is passed though the EO Space and JDS Uniphase EOMs in series.

We measured the inherent jitter from the input pulse driver system (Figure 3.5) by directing the escort laser onto two AEPX-65 fast photodiodes, one of which was delayed using a 200-ns delay cell (Section 3.3). The signal from the first was used to trigger a DG-535 delay generator that then triggered the pulse generator used to drive the EO Space EOM. The pulses from the Avtech pulse generator and the second AEPX-65 photodiode were used as the start and stop signals for a time-to-amplitude converter (TAC) and viewed on a multichannel analyzer (MCA). The FWHM for the full system was measured to be 82 ps. We also measured the jitter between two AEPX-65 photodiodes to be 12 ps, which

is not a significant contribution to the full system timing jitter.[3]

If we only used a single modulator to create our pulses, we found that the extinction ratio is only about 20 dB, and we would like it to be higher for making precision upconversion measurements. Most of the error comes from a ringing transient that follows the pulse; consequently, while the primary pulse shape is determined by the Avtech pulse generator driving the first EOM, we use the second EOM with a windowing pulse and a fast-fall time module (Stanford Research Systems DG-535 OPT-04B) connected to the DG-535 pulse generator to "mask out" the ringing effect created by the first modulator. The relative timing of the two pulses is controlled by programming the DG-535 delay generator, resulting in a consistent, 1550-nm Gaussian pulse with high extinction ($>$ 30 dB), synchronized to the 1064-nm escort pulse.

Once the 1550-nm pulse has been shaped, we pass it through a programmable attenuator capable of attenuating the beam up to 100 dB in 0.01-dB steps (JDS Uniphase HA9 Attenuator). However, in order for us to know how much attenuation is required to achieve the single-photon level, we must accurately measure the energy in a single 1550-nm pulse. We use a high-speed oscilloscope that has a fiber optic input (HP Agilent 83485A Optical Electrical Plugin in an HP Agilent 81000FA signal analyzer mainframe) to measure the pulse shape. The oscilloscope provides a direct measurement of the pulse shape, but careful analysis of the instrument revealed certain flaws. First, the scope has a bias of about -6 μW that must be subtracted off. Second, we noticed a consistent waveform oscillation that was present even with no signal attached to the instrument. We deduced that this ripple is intrinsic to the detector and eliminated it by measuring a trace without a pulse to obtain a trace of the inherent ripple, which we then subtracted from our pulse traces. Third, the traces produced had a small but significant amount of high-frequency noise caused by electrical noise in the instrument. A Fourier power spectrum of a trace without any signal attached reveals that this noise is all very high frequency, far above the response frequency of the optical diode. We concluded that this noise is intrinsic to the detector and may safely be removed from the signal using a Fourier frequency filter in post-processing (Figure 3.6). Finally, we need to calibrate how the power measured on the oscilloscope from the fiber corresponds to the power incident on the crystal in free space after exiting through a fiber-beam collimator, which we measured using a power meter (Newport 818-IR power head). By turning off the modulator, and applying a CW signal to the oscilloscope, then disconnecting the fiber from the oscilloscope and directing the light toward the crystal, we determined the correspondence between measured power and incident power.

[3]This jitter value was very sensitive to the trigger and output settings on the DG-535, and was minimized by setting the external trigger threshold to 0.20 V, using a positive trigger slope and 50Ω termination. The DG-535 output was set to 50Ω termination, amplitude of 2.00 V and an offset of 0 V.

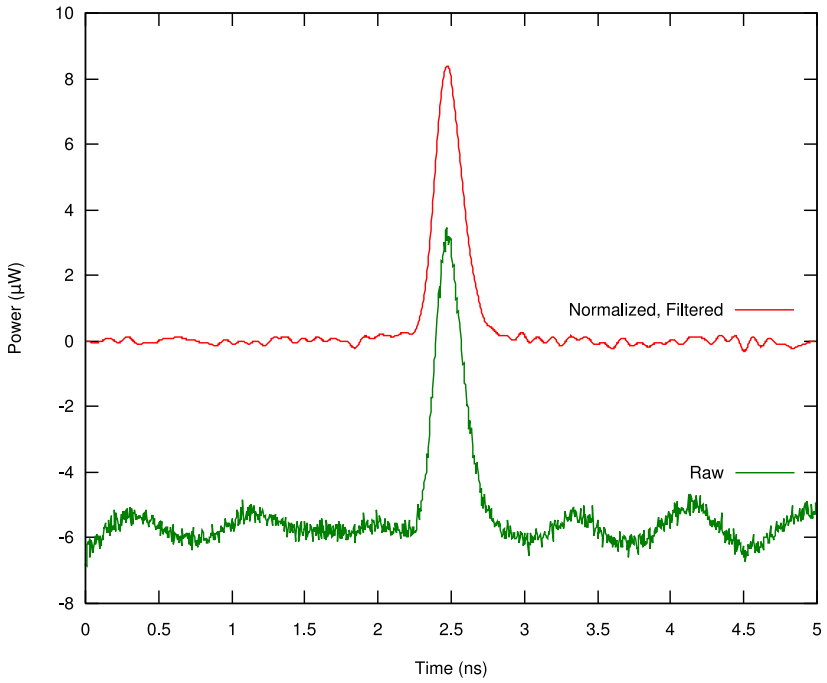

Figure 3.6: Comparison of the original oscilloscope trace of the input pulse with the post-processed pulse waveform. The post-processing removes detector offset, high-frequency noise, and systematic ringing in the detector, thereby providing a much more accurate estimate of the actual pulse shape.

3.5.1 Input Pulse Verification

In order to determine the repeatability of this pulse-creation procedure, we needed to estimate the error in calculating the area of the traces of the 1550-nm pulses on the Agilent oscilloscope. We took 10 traces (labeled 0-9) with no signal present over a domain of 5 ns, and a range of 160 μW, corresponding to 500 ps/div and 20 μW/div. Using a post-processing script (see Appendix B: process-pulse.scm) on traces 1-9, with trace 0 as the "background". This yielded traces which had the high frequency noise and systematic ringing removed. All that remained was mid-low frequency noise and 0-offset drift between traces. Another script (Appendix C) found an average value for these nine traces, integrated them from 0 to τ, and found the RMS of all nine integrals. We let τ vary from 0 to 5 ns. The RMS should have two main contributions: a part proportional to τ which comes from the shot-to-shot drift (a zero offset integrated over τ is proportional to τ) and a part due to the mid-frequency noise, which is proportional to $\sqrt{\tau}$ (since it is like a random walk away from 0). We fit the RMS data to the function $f(\tau) = A\tau + B\sqrt{\tau}$ and found $A = 8 \times 10^{-8}$ J/s and $B = 5^{-13}$ J/$\sqrt{\text{s}}$ (Figure 3.7). We solve for the τ where the two components are equal and found that the 0-offset error dominates for $\tau > 40$ ps, while the mid-frequency noise dominates for $\tau < 40$ ps. At 2 ns (our typical integration window when measuring pulse area) the uncertainty is 1.8×10^{-16} J.

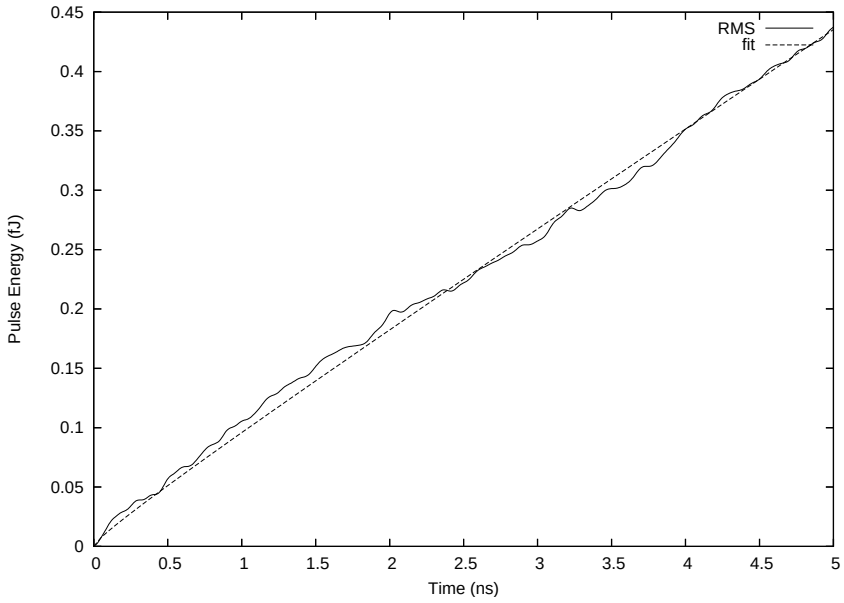

Figure 3.7: Measurement and fit of the error of pulse-area measurements as a function of integration time interval. Error originates from two sources: shot-to-shot systematic error and linear drift of v_0, the voltage required to balance the modulator. We find the former error dominates for times under 40 ps, while the latter dominates for longer time windows.

After determining the pulse area measurement uncertainty of our apparatus, we measured our 1550-nm pulse area. We took ten pulse traces and one dark trace. The biases on the EOMs were re-zeroed between each pulse trace to ascertain the repeatability of configuring the EOMs from scratch. After subtracting out the background and filtering the high-frequency noise (using process-pulse.scm; see Figure 3.6) we find an average pulse energy of 4.62×10^{-14}, with an RMS of about 2.5%. Since our measurement error of 1.8×10^{-16} J represents about 0.5% of this error, we can conclude that most of the pulse energy repeatability error is inherent to the pulse production system and not an artifact of the measurement. The most likely candidate for this error is the drift of the EOM biases. We repeated the pulse energy error measurement without rezeroing the EOMs in between measurements. The apparent pulse energy increased linearly with each each trace over five successive traces at a rate of 4.5×10^{-16} J/min or about 0.7%/min, and the extinction ratio drifted 0.26 dB/min. This is consistent with the 2.5% reproducibility in the pulse generation since each trace measurement lasted ∼4 minutes when we were rezeroing the EOMs every time. EOM bias drift as a source of error could be greatly reduced by actively stabilizing the modulators.

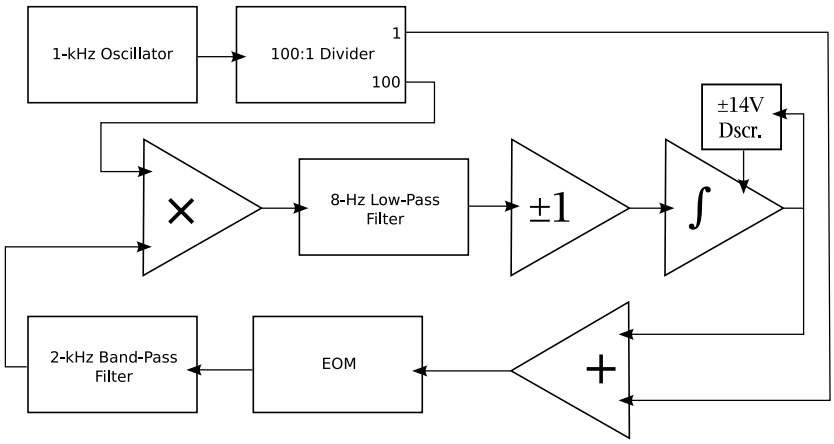

Figure 3.8: Bias feedback control circuit for electrooptic modulator. A 1-kHz dither signal modulates the bias voltage of an EOM. The resulting 2-kHz photosignal is modulated with the 1-kHz clock and averaged over 120 ms to determine if the current bias is too high or low. The signal is then fed back into the integrator, which maintains the bias with the correct feedback sign (positive or negative), determined by a switching inverter to maintain minimum or maximum EOM transmission.

3.5.2 Bias Control

To counteract the drift in the phase of the EOMs, we designed a feedback circuit to monitor the light transmitted by the EOM and make adjustments to the applied voltage bias, maintaining the EOM near the point of maximum extinction. The circuit operates by generating a 1-kHz sinusoidal clock signal with a 1-V amplitude and voltage-dividing it by a factor of 100 to generate a 10-mV signal that is synchronized with the clock. This attenuated dither signal is added to a voltage register storing the current bias and applied to the EOM. We detect the optical signal using the photodiode integrated into the EOM package. The photodiode signal p is given by

$$p(v_b) = \sin^2[(v_b - v_0)\pi/v_\pi], \tag{3.1}$$

where p is the photodiode signal, v_b is the bias voltage applied to the EOM, v_0 is the bias voltage at which the EOM has maximum extinction, and v_π is the voltage required to shift the phase of the EOM by π. If $(v_b - v_0)$ is small, p approximates the square of the dither signal, yielding a 2-kHz sinusoidal oscillation. We use a 100-Hz wide band-pass filter centered at 2 kHz to remove other sources of modulation, such as the 200-ps input pulses, and isolate the component of the photodiode signal generated by the dither signal. We then multiply this signal with the original unattenuated clock signal and filter the multiplied signal with an 8-Hz low-pass filter, which effectively takes a time average of the multiplied signal over a 120-ms window. This time average A is

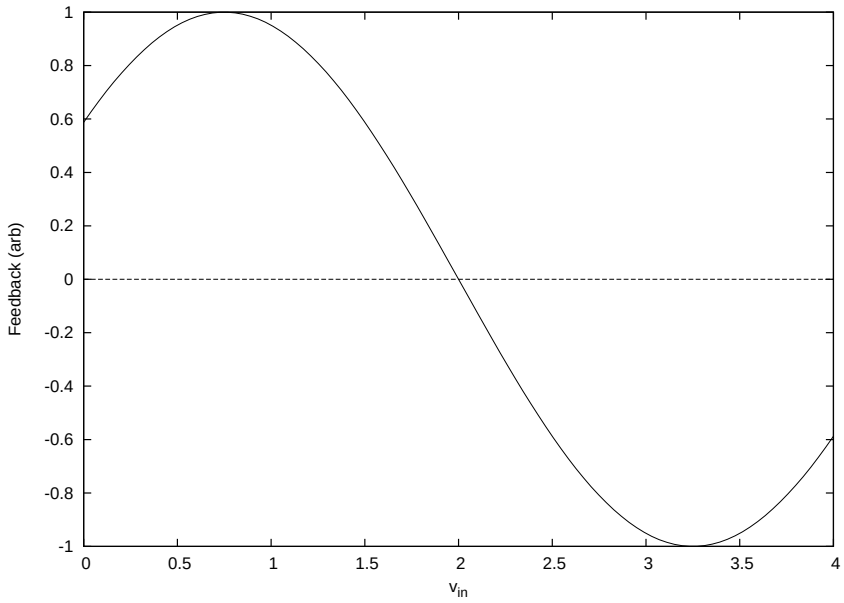

Figure 3.9: Numerical model of feedback dependence of the bias control circuit, with $v_0 = 2$ V and $v_\pi = 5$ V. We observe that when v_{in} is greater (less) than v_0 the feedback is positive (negative).

computed by

$$A = \int_{0\,\mathrm{ms}}^{120\,\mathrm{ms}} c(t)p(v_b + \delta(t))dt, \tag{3.2}$$

where $\delta(t)$ is the dither signal and $c(t)$ is the clock signal. The quantity A is zero when $v_b = v_0$ and the 2-kHz peaks of p are all equal. However, when the peaks of p coinciding with the positive segments of the 1-kHz c are higher than the peaks of p corresponding to the negative segments of c, A will be positive. Inversely, A is negative when the highest peaks in p correspond to the negative portions of c. Consequently, A indicates whether we should increase or decrease v_b to force it to equal v_0. We feed A back into an integrator using a switchable inverter to determine if we would like to hold the bias at a signal maximum or minimum. This integrated value is then fed back into the system as the new v_b. As a safety precaution to protect the EOM, we also included a discriminator that shorts the register capacitor in the integrator if v_b strays outside the range ± 14 V.

We designed a constructed a circuit to implement the above feedback bias control device, and preliminary data suggested it could successfully maintain a signal minimum. Unfortunately, the integrated photodiodes in the EOMs were destroyed by electrostatic discharge before the device's capacity for generating input pulses could be fully characterized. We designed a photodiode protection circuit (Figure 3.10) that should prevent such difficulties in the future, should the EOM integrated diodes ever be replaced.

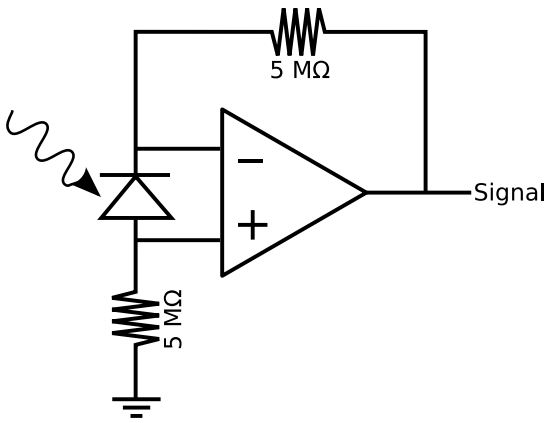

Figure 3.10: Circuit for amplifying and protecting the diode [1]. The feedback on the operational amplifier is configured to maintain the voltage across the diode at 0 V, independent of the photo current passing through the diode. The signal output is highly linearly related to the intensity of light incident on the diode, improving the feedback circuit responsiveness.

3.6 Mode Alignment

Precise alignment of the spatial modes of the input and escort beams is critical for high-efficiency upconversion. We would like the two beams to be coaxial, but the input to have a tighter focus than the escort so that the latter field is approximately uniform over the input beam. We begin by directing the escort beam though a dichroic beamsplitter and toward the eventual location of the crystal. We use achromatic lenses in Z-axis positioning mounts that allow us to change the focus size and location of the escort without changing the central ray vector. We use a beam profiler (Gentec EO BeamScope-P9) to measure the spot size of the attenuated escort. We measure the the escort at the position which corresponds to the center of the crystal, compensating for the different index in free space, so that when the crystal is installed, the escort will focus in the crystal's center.

Once we have created a 200-μm spot in the correct position, we direct the input beam into the system by reflecting it off the dichroic beamsplitter. We use the dichroic beamsplitter in reflection for the input and transmission for the escort since the reflection mode has lower loss than the transmission mode. The input is focused to an 80-μm spot centered on the focus of the escort. All of the focusing is done upstream of (i.e., before) the dichroic beamsplitter, so chromatic dependencies in the strength of the lenses are irrelevant and laser-line antireflection coatings appropriate for each of the two beams may be used to minimize losses. Since tilting the dichroic beamsplitter to steer the input parasitically alters the escort beam through walkoff, even in transmission mode, we manipulate the input beam using a tilt mount for the laser's fiber-to-free space coupler to control the k-vector, and a tiltable antireflection-coated glass

window to control the lateral displacement through walkoff. We also include a HeNe guide laser, matched to the escort with another dichroic beamsplitter. Since the wavelength of the escort (1064 nm) is shorter than the input (1550 nm), and the guide laser wavelength (633 nm) is shorter still, the guide laser beam is transmitted through the short-pass dichroic beamsplitter used to combine the input and escort pulses. The HeNe guide laser has a wavelength of 633 nm, very close to the 631-nm output beam and thus the guide laser can be used to align the output collection optics. Furthermore, the guide laser is useful for roughly aligning the crystal, as both the 1064-nm escort and 1550-nm input beams are invisible to the naked eye.

Once we focused and combined the beams, we installed and positioned the crystal. The 4.5-cm long PPLN crystal (HC Photonics Custom 11-12-μm Multi-grating PPLN with 631/1064/1550-nm AR Coating) is mounted in an oven to allow temperature tuning of the phasematching conditions. The oven is in turn mounted on a positioning stage (NewFocus 9082 Wide Five-Axis Aligner) that has been set on a lab jack (ThorLabs LJ750 Compact Lab Jack) for height adjustment. The crystal is 0.5 mm thick and 5 mm wide, with six 0.8-mm wide poled channels. Each channel has a different poling period; however, we only consider the channel with the 11.4-μm poling period. It is important to have both beams aligned straight down the center of the channel axis; if the crystal is displaced off center, there can be losses from clipping on the top or bottom of the crystal and sides of the poling channel. If the crystal is canted, the beams will refract at slightly different angles on the input face of the crystal and will not completely overlap in the center–even though the two beams were well centered in free space– and the conversion efficiency will be adversely affected. In practice, this also means we must make sure the crystal face is highly perpendicular to the channel axis. The first crystals we obtained had faces about 1° away from perpendicular, a tolerance which proved insufficient. We had the crystals re-diced to 5 minutes of arc (1.5 mrad), allowing us to easily overlap the beams inside the crystal.

The tilt and yaw of the crystal are controlled using the five-axis aligner. To obtain a high level of alignment between the escort beams and the channel axis, we first back-reflect the guide laser off the input face of the crystal. This is only sufficient for a crude alignment, however, since the available moment arm for back-reflecting is short, limiting the precision to a degree or so. To obtain higher accuracy alignment, we use the five-axis aligner to intentionally adjust the yaw (about the Y-axis) of the crystal a small amount. We observe either the 633-nm guide laser or the 532-nm light (created from unintentional second harmonic generation of the escort as it passes though the crystal) as it is projected on a card placed behind the crystal. As we translate the crystal back and forth in the x-direction, we notice a secondary spot appear on the card next to the primary laser spot of the guide laser. The secondary spot is created from the light reflecting off the the side of the channel where a small refraction index

boundary is created from the induced internal stress that appears when ferroelectric domains meet, a product of the periodic poling process. The direction of this secondary spot indicates the yaw of the crystal. If the secondary spot is in the positive-x direction, we must rotate the crystal about the y-axis so the exit face moves in the negative-x direction, and vice versa. Once we can translate the beam across the complete channel without producing secondary spots on either side, we consider the crystal to be properly aligned. We then repeat this procedure on the tilt axis (about the x-axis) by translating through the y-axis and looking for secondary reflections above or below the primary spot. Note that these alignments must be done at or close to the desired phasematching temperature, since thermal expansion can cause the alignment to change.

3.7 Low-Loss Filtering

After aligning the crystal, we set up the acquisition system and performed final tuning. We performed the following steps to reduce the significant background from the 1064-nm escort laser and the 532-nm second-harmonic light. We used a high-transmission (transmission $> 93\%$) filter centered near 631-nm (Semrock CY5 Emitter Filter) to reject most of the remaining 1064-nm escort and 532-nm second-harmonic-generated light. This filter is placed close to the exit face of the crystal, and is tilted at a slight angle to prevent the escort light from traversing back down the crystal channel. Otherwise, a cavity situation may be established where the escort makes multiple trips through the crystal, which could artificially inflate some of our results. We must be careful not to tip the filter too much, however, or else the apparent transmission wavelength window will occlude the 631-nm output photons. Next, a 100-mm lens is used to refocus the output beam through a halfwave plate at 45°, which rotates the polarization of the output light from vertical to horizontal. We require horizontally polarized light to take advantage of the Brewster-angle dispersion prisms that follow the collimation lens (see Figure 3.1).

To align the dispersion prism for maximum transparency and wavelength separation, we placed a white index card to the side of the prism and minimized the reflected guide light by rotating the prism. We placed an iris on the far side of the prism with a $\sim$3-mm opening near the focus of the beam created by the lens. We attached a 10-nm wide interference filter centered at 633 nm to a power meter (Newport 818-SL Power Head) to eliminate the room light and measure the upconverted light[4]. Once the upconverted light was detected, we attenuated the escort light more than an order of magnitude so as to ensure that the peak escort intensity was not causing overconversion (see Section 5.4), and then optimized the temperature for maximum conversion.

[4]We found it was important to read the power head using a Newport 1835-C power meter instead of a Newport 840-C handheld power meter, since the former is much more sensitive to the sub-nW power levels typical of the system when not precisely phasematched.

We next removed the power meter and configured a *second* Brewster-angle dispersion prism and iris. We positioned the second prism to refract the beam in the same direction as the first so as not to undo the frequency discrimination performed by the first prism. After the second prism stage, we direct the light into a box constructed of aluminum plates and covered with a rubberized black fabric shroud. The box contained a final interference filter, an achromatic 30-mm lens to focus the light to a $\sim$20-μm spot size, and a silicon APD single-photon detector (Perkin Elmer SPCM-AQR-14). The detector was mounted on a three-axis translation stage (Newport Series 462 ULTRAlign Precision Linear Stage) to optimize the detection of single photons by positioning the detector's active area in front of the focusing lens. Using this system, we were able to maintain a high detection efficiency while simultaneously achieving an escort extinction ratio of $> 10^{15}$.

3.8 Efficiency Results

After the PPLN, and the filtering setup, the upconverted photon detected using a silicon (APD). By knowing the initial rate of IR photons, and the collection and detection efficiencies of our system, we can determine the net conversion efficiency. With this system, operating at $\sim$40 kHz, we have obtained conversion efficiencies of up to $99 \pm 4\%$, and system detection efficiency of $56 \pm 2\%$. As discussed previously, the main contributions to the uncertainty is the error in measuring the 1550-nm input pulse area. In addition, the conversion efficiency uncertainty is higher than the detection uncertainty because it is also affected by uncertainty in the efficiency of the filtering system, as well as the uncertainty in the quantum efficiency of the silicon APD.

We required an escort pulse energy of $\sim$2 μJ to achieve high-efficiency conversion. This intense escort produced a significant amount of background at both 1064 nm as well as 532 nm. Additional background was produced by Raman scattering of the escort at 1550 nm that upconverted to 631 nm. Using filters and prisms, we were able to reduce the background to 10^{-2} counts per pulse at the highest conversion efficiency. We observed background much higher than this at one point; however, this was discovered to be damage to the crystal (see Appendix D). By attenuating the escort below 1 μJ, and decreasing the escort spot size, we observed the background drop to 3×10^{-3}, however, the conversion efficiency also dropped to $\sim$96%.

4 Coherent Upconversion

4.1 Coherence Introduction

Having shown that high-efficiency conversion of single-photons is possible using frequency upconversion, we must also show that the process is coherent for it to be useful for quantum information applications[1]. There are two classes of possible *incoherent* processes that are consistent with the previously observed high-efficiency upconversion data. These must be excluded before upconversion may be used to operate coherently on photonic qubits. The first process is a measurement process. If the process of upconversion performs a projected measurement on the photon, collapsing it into an eigenstate in the photon number basis, then any quantum information encoded onto the photon would be destroyed during the conversion process. We can imagine the PPLN crystal in the high-efficiency experiment could be replaced by a single-photon detector coupled to a single-photon emitter that is powered by the escort beam. Such a device could be designed so that the combined probability of detecting a single 1550-nm photon and emitting a 631-nm photon had the observed dependence on escort power. By measuring the photon, this type of device would produce a statistical mixture of photons at the two different frequencies and not a superposition, as required for quantum information applications. Any phase or entanglement relationships possessed by the input photon would not be preserved in the output photon. Although such a scenario is highly unlikely, the data observed so far [20] cannot rule out such a possibility.

The second class of processes we must eliminate are noise-introducing processes. In this scenario, the input photon would be converted to the output frequency in a measurement-free manner; however, an additional random phase is applied to the converted photon. Potential sources of noise could be artifacts of the apparatus (e.g., thermal or vibrational fluctuations in the crystal) or intrinsic to the quantum transduction process itself. This phase noise would be fatal to an upconverted qubit, since it would start as a pure state and end up a completely mixed state, destroying any quantum information.

Not surprisingly, these two scenarios, though they arise from different mechanisms are actually equivalent. In the absence of ancillary information, a classical statistical ensemble of input and output photons is indistinguishable from a set of photons which are a superposition of input and output wavelengths if the two

[1] Section in this chapter reproduced from [34]

components of the superposition have no definite phase relationship.

To close this "coherence" loophole, we must experimentally confirm that there is a definite phase relationship between the input and upconverted photons. This is accomplished by preparing a photon in a superposition of two time-bins, upconverting each one independently, and measuring interference fringes between the two upconverted time-bin components. If the frequency conversion process does not measure the photon, and preserves the phase relationship between the two time-bin components, we will have demonstrated quantum coherence and may certify the process as "zero quantum noise" and suitable for use on qubits.

4.2 Experimental Setup

To investigate the coherence of the upconversion process, we send both a 1550-nm photon and the escort pulse through an unbalanced interferometer (Figure 4.1a shows this process using unbalance Mach-Zehnder interferometers for clarity). The path-length difference of the long and short arms (1.4 m) is much greater than the pulse width of both the escort (600 ps) and 1550-nm (200 ps) pulses. In this way we prepare a coherent superposition of two time-bins [21] for the 1550-nm photon. After upconversion of the photon amplitude in each time-bin, we use a second interferometer to verify that the upconversion process preserved the phase coherence between the time bins. The exiting upconverted photon can be detected at one of three possible times. The earliest (latest) arrival times correspond to distinguishable events where the photon traveled the short (long) arms on both trips through the interferometer. The short-long and long-short processes contributing to the middle time-bin will interfere if, and only if, the upconversion process preserves the coherence of the time-bin qubit.

For our experiment we used a double-pass Michelson interferometer (Figure 4.1b,c). We first focus both beams onto a "virtual waist" 15 cm before the interferometer beam splitter. The (spherical) end mirrors on each arm image this virtual waist onto the center of a 1.5-cm crystal, allowing both beams in both arms to be focused onto the same point (for this experiment they all had approximately the same spot size, $\sim 60\,\mu$m). The upconverted output at 631 nm is directed through an identical unbalanced interferometer; for stability we simply reflect the photon back through the *same* crystal and interferometer (a filter removes the other wavelengths), so that any path-length fluctuations affect both the "short-long" and "long-short" processes identically. Upon re-exiting the interferometer, the 631-nm light is separated out from the remaining escort light using a dichroic beam splitter, dispersion prisms, and interference filters.

We use folded Michelson interferometers instead of two separate Mach-Zehnder interferometers as the Michelson design is self-stabilizing. If, for example, the long-arm end mirror displaces an amount Δx, it adds an additional phase $\phi_1 = \Delta x/\lambda_o$ to the short-long process, and a phase $\phi_2 = \Delta x/\lambda_i + \Delta x/\lambda_e$

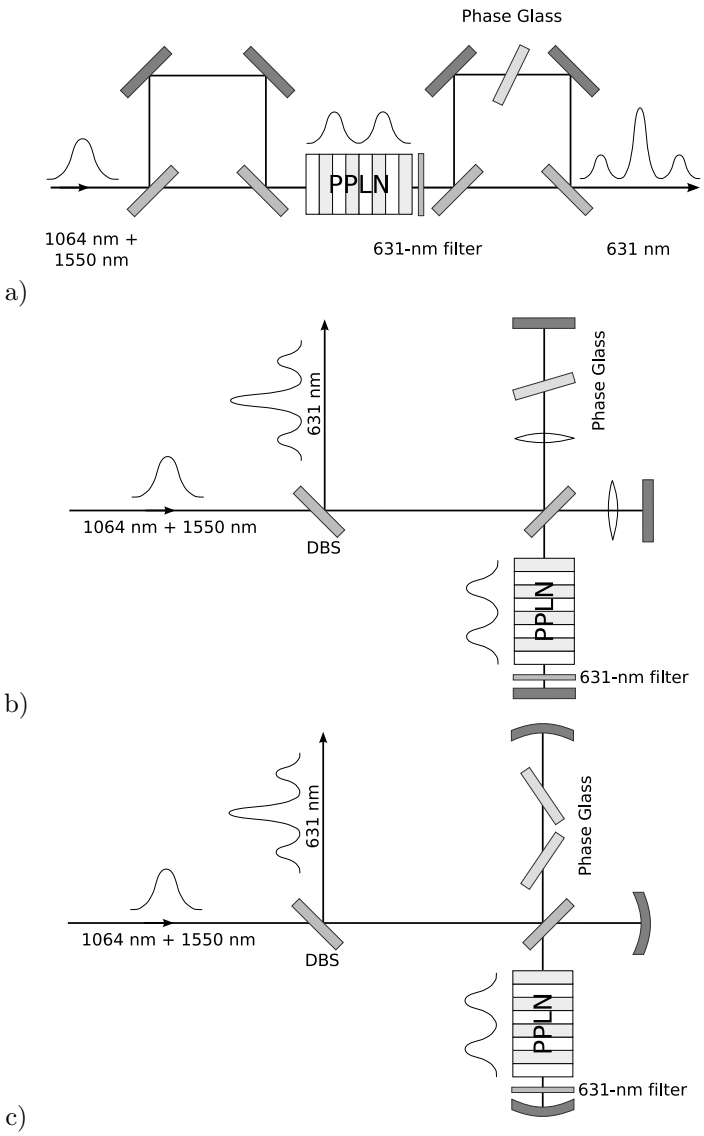

Figure 4.1: a) A 1550-nm pulse is prepared along with a bright 1064-nm escort pulse in a two-time-bin superposition state using an unbalanced Mach-Zehnder interferometer. The photon is upconverted and then passed through another interferometer with a phase shifter in one arm. Interference fringes are observed in the resulting middle time-bin. b) An equivalent, but more robust, implementation using an unbalanced Michelson interferometer. After the two time-bin state is prepared and upconverted, it is reflected back through the interferometer, and picked off using a dichroic beam splitter where it is detected by an APD. Lenses in the arms focus onto flat end mirrors, effectively time reversing the beam. A dispersive glass plate is tipped to control the phase between long-short and short-long processes. c) Curved mirrors at the ends of each arm are used to time-reverse the beam, and the single glass plate is replaced by two dispersive glass plates that are tipped near Brewster's angle to produce a low-loss and zero-walkoff phase shift between the long-short and short-long processes.

to the long-short process. However, due to the conservation of energy relationship (Equation 1.5), ϕ_1 is precisely equal to ϕ_2, so the total phase difference between the long-short and short-long processes for a displacement of Δx is zero. This arrangement is so stable that we were able to obtain high-visibility interference fringes without the use of a floating optical table, and despite a significant source of acoustic vibrations in the room.

Another advantage of the folded, unbalance Michelson scheme is that it is always exactly balanced. The precise reflectivity of the central beamsplitter at the three wavelengths is unimportant since both the long-short and short-long processes each have one reflection and one transmission at each of the three wavelengths λ_i, λ_e, and λ_o. With most interferometer designs, it is important to use beamsplitters that have reflectivities near 50% to achieve high visibility. With our design, while it is desireable to use a beam splitter with roughly 50% reflectivity at all three wavelengths to maximize signal amplitude, the signal visibility does not depend on the reflectivities of the beamsplitter.

We initially constructed the arms of the interferometer with a lens (50 mm for the short arm, and 100 mm for the long arm) to refocus the beam, and a mirror placed at the focal point of the lens (Figure 4.1b). Since the phase-front is flat at the waist, and the mirror is flat, the reflection should perfectly time reverse the beam and cause it to overlap the same mode all the way back to the beamsplitter. The modes from both arms then recombine at the beamsplitter and overlap perfectly–although with different time delays. The virtual waist is then mapped onto the center of the crystal via two different paths: the long and short arms of the interferometer.

To see fringes we must be able to control the phase of one arm relative to another. We placed a microscope slide on a rotation stage between the lens and the mirror in the long arm. Since the glass is dispersive, by tilting the slide, we were able to create a phase difference between the long-short and short-long processes. A second slide was placed in the short arm so that the two arms had balanced transparencies. Using the lens-mirror time-reversal arrangement, we note that transverse movements of the beam do not affect the mode of the waist in the crystal, since the mirror is flat, and displacing where it meets the beam has no effect. This scheme worked reasonably well (Figure 4.2), however was ultimately limited in visibility to about 90% by limitations with the phase-control mechanism. The microscope slides were wedged slightly and so tilting them changed not only the walkoff, but the k-vector as well, which meant that the waist inside the crystal propagated from the long arm would move slightly relative to the waist from the short arm. Without consistent mode overlap between the two arms, we were limited in the interference visibility.

A second difficulty with this scheme was the static mode-matching problem. Aligning this interferometer requires six modes at 3 different wavelengths to all overlap with interferometric precision. The controls of these modes are highly coupled, since moving any of the two lenses or two mirrors will affect all of

the beams simultaneously. Dispersion in the lenses cause the degree to which each mode is affected to be different for each wavelength. We realized that an achromatic system for time reversing the beams at the end of the arms would perhaps allow a simpler system of alignment. We replaced the lens-flat mirror setup with a simple curved mirror (Figure 4.1c) that had a radius of curvature equal to the distance between the end mirror and the beam waist in the crystal (1 mm for the long arm, and 30 cm for the short arm). This arrangement yielded only two achromatic degrees of freedom per arm, rather than four chromatic and two achromatic degrees for the lens-mirror case, greatly simplifying alignment of the interferometer.

The drawback of this arrangement is that tilting the microscope slide was no longer an option, since a transverse displacement of a beam impacting on a curved mirror would affect the direction and disturb the eventual waist position in the crystal. We developed a system of adding phase to one path without displacing the beam. We used two 1-mm thick glass optical flats, which were post-selected by the manufacturer (CVI Laser) to find a matched pair that were both highly parallel and of equal thickness to a tolerance of 1%. These two flats were placed in rotation stages at supplementary angles (the angles between the beam and the plates should sum to 180°) so that any walkoff caused by the first flat would be canceled by the second. Also, rather than placing a second pair of flats in the short arm to balance the transmission, we tilted the flats to be close to brewsters angle. This gave us nearly unit transmission, even after the eight passes through the flat (two flats × two passes on each round trip down the long arm × two processes–long-short and short-long). We were more limited by the range of angles through which the flats could be tipped without disturbing the mode. However, since the flats were thicker than the microscope slides, and we had two of them, and we were going through them at oblique angles, the tilt required per degree of optical phase shift was much smaller. Using this scheme, we were able to achieve higher visibility, as discussed below.

4.3 Coherence Results

The phase is controlled by tipping two 1-mm thick glass plates in the long arm. The glass is dispersive, and in each process different wavelengths pass through the glass, causing a relative phase shift between the short-long and long-short processes given by

$$\Phi(\theta) = 4\pi p d \left(\frac{\xi_{n_i}(\theta)}{\lambda_i} + \frac{\xi_{n_e}(\theta)}{\lambda_e} - \frac{\xi_{n_o}(\theta)}{\lambda_o} \right), \tag{4.1}$$

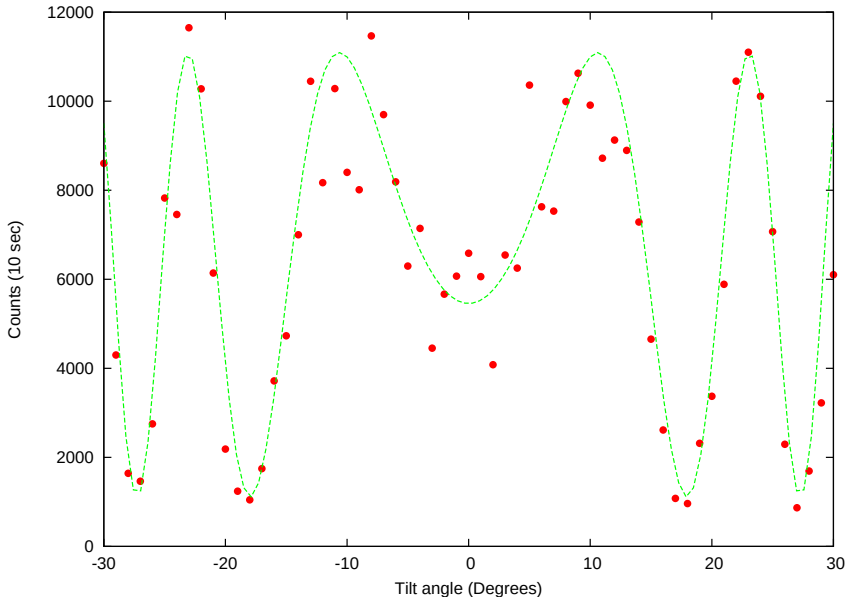

Figure 4.2: Coherence fringes along with a fit of the fringes. The fit was based on a calculation of the phase induced by tilting a microscope slide of known thickness and dispersion function. The fit has only two free parameters, the visibility and the initial phase. Though the overall character of the fit is confirmed, the counts fluctuate more than we would expect from counting statistics. We attribute this to nonuniformity in the microscope slide.

where p is the number of glass phase plates, d is the thickness of the plates, θ is the angle of the first phase plate, and $\xi_{n_j}(\theta)$ is given by

$$\xi_{n_j}(\theta) \equiv \frac{n_j - \cos(\theta - \sin^{-1}[\sin(\theta)/n_j])}{\cos(\sin^{-1}[\sin(\theta)/n_j])} + 1 - n_j. \tag{4.2}$$

Figure 4.3a shows the time histogram of the detected photons for two extremal values of the phase shift. Figure 4.3b shows the number of photons detected versus the angle of the phase-glass, along with a theoretical fit using only the initial phase and visibility as free parameters. The fit visibility is $95 \pm 1\%$, without subtracting background counts, indicating that the transduction process indeed preserves the coherence of the time-bin qubit. Similar time-bin conserving upconversion has also recently been demonstrated using PPLN waveguides [21]; however, waveguide coupling losses limited the net-conversion efficiency to less than 10%.

This two-time bin encoding is precisely that used by most fiber-based quantum cryptography efforts [19, 24, 29, 30, 31], which, moreover, also rely on attenuated pulses to approximate single-photon states. Our present level of interference contrast would correspond to an approximate key distribution bit error rate of 2.5%, comparable to that reported with existing systems. Note also that in principle these upconversion methods can allow superior detection

time resolution, limited only by the escort pulse duration, and not the detector response jitter.

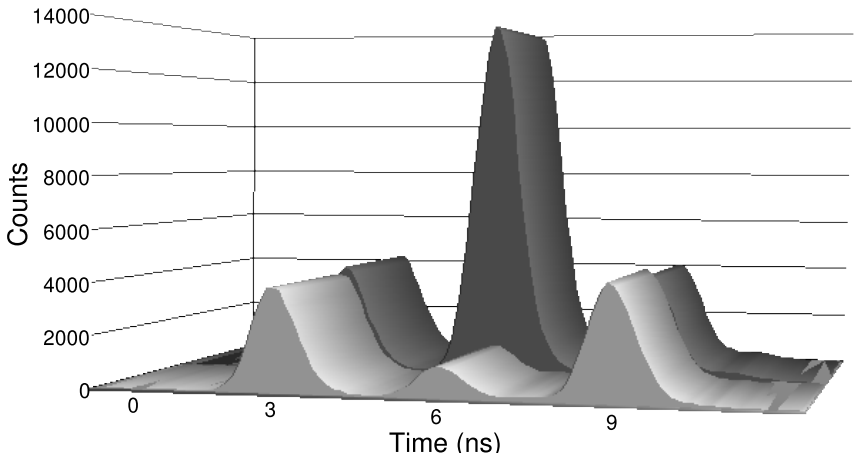

a)

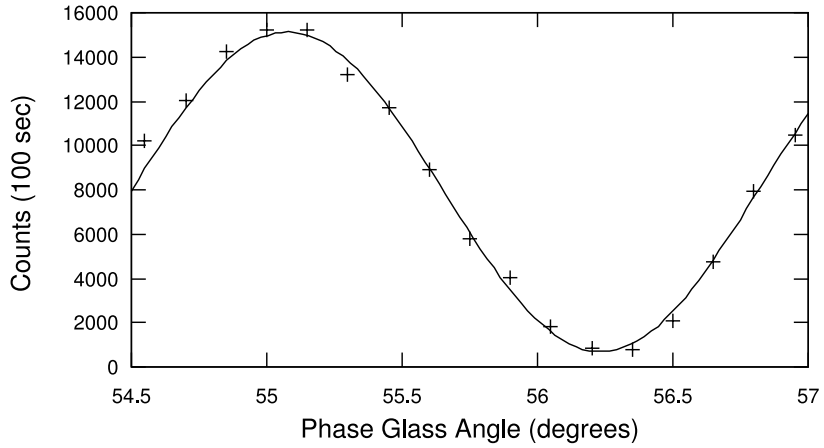

b)

Figure 4.3: a) Detected photons versus time for two settings of the phase glass, corresponding to constructive and destructive interference. The long-long and short-short processes are unaffected by the position of the phase glass, while the central time-bin, arising from the interfering short-long and long-short processes, varies greatly. b) Number of photons detected in the central time bin as the phase glass plates are tilted. The 95%-visibility fringe demonstrates the coherence of the upconversion process.

5 Rabi Oscillations

5.1 Introduction

Rabi oscillations are an important phenomenon in quantum mechanics. The combination of full Rabi oscillations and phase operations represents the complete group of arbitrary rotations in a two-dimensional Hilbert space. This allows us to perform any non-decohering single-qubit operation. We observe an escort beam ($\lambda_e = 2\pi/\omega_e$) used to upconvert a photon from an initial, long wavelength ($\lambda_i = 2\pi/\omega_i$) to a shorter wavelength ($\lambda_o = 2\pi/\omega_o$) will then down-convert the photon back to the initial wavelength. This continual oscillation between low and high energies, driven by the escort beam, is remarkably similar to the Rabi oscillation of an atom, where the energy states of the atom are driven by an applied radiation field. By mimicking the dynamics of an atom with a photon, we hope to observe the rich set of behaviors seen in atomic physics manifest in photons, as well as gain insight into atomic physics by experimenting with photons[1].

5.2 Theory of Photon Rabi Oscillations

When we solve the reduced field equations (equations 1.7 and 1.8), we observe a striking similarity with the dynamics of an atomic Rabi system where radiation of strength γ and frequency ω excites a transition with frequency ω_{21}. In an atomic system, the atom has certain probability amplitudes, c_1 and c_2 to be found in each of the two energy states. The probability of finding the state in state c_2 is [32]

$$|c_2(t)|^2 = \frac{\gamma^2/\hbar^2}{\gamma^2/\hbar^2 + (\omega - \omega_{21})^2/4} \sin^2\left[\left(\frac{\gamma^2}{\hbar^2} + \frac{(\omega - \omega_{21})^2}{4}\right)^{1/2} t\right]. \tag{5.1}$$

If we make the following simple substitutions

$$\frac{\gamma^2}{\hbar^2} \rightarrow \frac{\omega_i \omega_o d_Q^2}{n_i n_o c^2}|E_e|^2 \tag{5.2}$$

$$\omega - \omega_{21} \rightarrow \Delta k_Q \tag{5.3}$$

$$t \rightarrow z \tag{5.4}$$

[1] Sections in this chapter reproduced from [34]

that represent the photon analogues for interaction strength (5.2), detuning (5.3), and propagation dimension (5.4), we obtain the solution for the nonlinear field evolution equations 1.1-1.3:

$$P_o(z) = \left[1 + \left(\frac{\Delta k_Q^2}{4}\right)\left(\frac{n_i n_o c^2}{\omega_i \omega_o d_Q^2 |E_e|^2}\right)\right]^{-1} \sin^2\left[\left(\frac{\omega_i \omega_o d_Q^2}{n_i n_o c^2}|E_e|^2 + \frac{\Delta k_Q^2}{4}\right)^{1/2} z\right]. \tag{5.5}$$

Thus we predict we can reproduce Rabi-like oscillations in a nonlinear crystal by driving a photon between ω_i and ω_o using an escort field at frequency ω_e.

5.3 Indirect Observations of Photon Rabi Oscillations

Our first attempt to demonstrate upconversion used a 1064-nm passively Q-switched Nd:YAG laser which produced 600-ps pulses (Figure 5.1) at a rate of 7.2 kHz. This was combined with a 400-ps 1550-nm input pulse, which we attenuated to near the single-photon level. The input pulses were electronically triggered with a timing resolution of a few picoseconds. The pump, however, had a pulse-to-pulse jitter which, at a few microseconds, was much longer than the escort pulse duration. Even though the input pulse is triggered off of the previous escort pulse, after a suitable delay, this prohibited exact synchronization of the two pulses. Instead, we measured the relative delay between a pair of input and escort pulses, and occasionally, when this delay is near zero, there is a chance for the input to be upconverted. When we detect the upconverted photon, the delay that produced the upconversion event is not recorded (only delay events which do *not* produce an upconversion event are recorded). We obtain a histogram of the distribution of relative delays, with the delays that produce upconversion suppressed. By subtracting this histogram from the baseline distribution of input-escort delays, we obtain the relative probability of conversion for various delays. We notice that the probability of conversion when the pulses are completely overlapped is *lower* than when most of the input is exposed to intensities less than the maximum, indicating that at the peak of the escort, the input is completely converting to the higher frequency and then partially overconverting back to the lower frequency.

At the beginning of the pulse cycle (Figure 5.3; Table 5.1), a 1064-nm Nd:YAG laser fires a pulse that sends an electrical trigger signal to an Ortec 593 constant fraction discriminator (CFD). The discriminator sends out two simultaneous TTL pulses, one of which triggers a Stanford Research Systems DG-535 programmable delay generator labeled "A". The other pulse from the discriminator is routed to a time-to-amplitude converter (TAC) for use with the previous cycle. As explained below, the following YAG pulse will generate the TAC "stop" pulse used for this cycle. Delay generator A then waits 100 μs be-

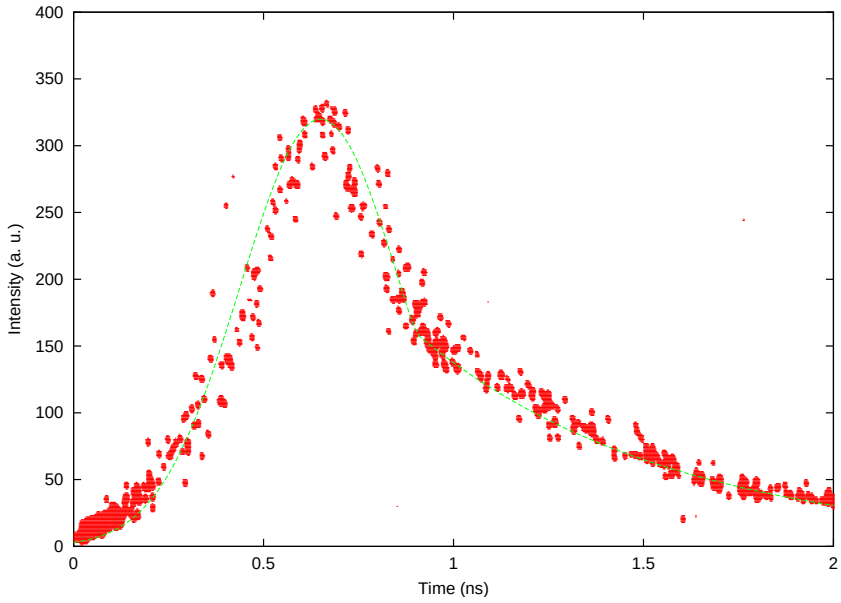

Figure 5.1: Analog sampling oscilloscope trace of the 7.2-kHz 1064-nm 50-mW Nd:YAG laser (JDS Uniphase NP-00321-110) along with a fit. The fit function used is a Gaussian pulse with an exponential tail.

fore sending out another TTL pulse to a second DG-535 delay generator labeled "B," which sends signals to the "start" channel of the TAC, and the Avtech picosecond pulse generator (Avtech AVP-2S-C-P-UILB pulse generator) 36 μs and 37 μs after the delay generator receives the trigger pulse, respectively. Two delay generators are required to break up the 137-μs delay between consecutive YAG pulses: if a single delay generator were waiting for the full 137-μs duration, it would be preoccupied with counting, triggering, and resetting and would be unable to process the latter pulse. Splitting the delay into two pipelined delays allows the sum of the programmed delay and reset time of each delay generator to be less than the period of the YAG laser driving the experiment.

The Avtech picosecond pulse generator creates a short 200-ps pulse which drives the JDS Uniphase H501 electrooptic modulator (EOM) driver that, in turn, drives the JDS Uniphase X5 EOM. The light from a 1.3-mW 1550-nm fiber-coupled diode laser is passed through the EOM, which has been voltage biased for minimum transmission when the Avtech pulse generator is off. A 300-ps pulse (Figure 5.2) emerges from the modulator and is attenuated to the single-photon level (JDS Uniphase HA9 fiber attenuator) at approximately the same time as the next 1064-nm escort pulse is emitted from the YAG laser. Since the 1550-nm pulse is synchronized to the previous escort pulse, with an additional 137-μs delay (the mean period of the escort laser), the distribution of relative delays between the input and escort lasers is simply determined by $\langle\sigma\rangle \approx 2$ μs, the jitter of the YAG laser. If σ is close to zero, the input photon will coincide with the next escort pulse and be upconverted into a 631-nm output

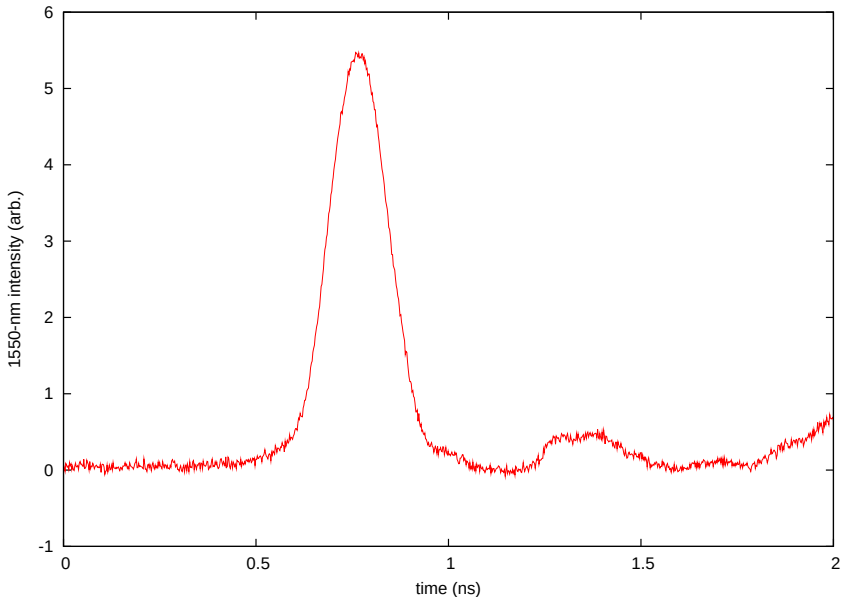

Figure 5.2: Oscilloscope trace of a 1550-nm laser pulse that was shaped by passing the light from a CW 1550-nm telecommunications fiber-coupled laser diode through an electrooptic modulator driven by an Avtech electrical pulse generator.

photon using a 4.5-cm PPLN crystal. The upconverted photon will then be detected by a silicon avalanche photodiode that, upon detecting a photon, sends an inhibit signal to the TAC.

The TAC records the delays (σ) between start (input) and stop (escort) signals that are not inhibited by an APD detection event and sends them to a multichannel analyzer (MCA). We are encouraged by the design of the TAC to record non-upconverted delays instead of upconverted delays. The TAC's inhibit logic is such that it order to record a particular delay, the inhibit signal must be low 10 μs before the start pulse, and remain low through both start and stop pulses. Since we cannot predict upconversion events that far in advance of the start pulse, we cannot configure the system to default to inhibited operation while having the APD signal enable the TAC to record the pulse. Instead we default to record everything, since we are able to quickly interrupt recording the delay when the APD fires.

The data from this indirect measurement of Rabi oscillations is plotted in Figure 5.4. We plotted the escort pulse and its corresponding conversion profile (Equation 5.5 applied to the escort profile) against a histogram of relative delays between the signal and escort pulses which produced upconverted photons. The height of the histogram corresponds to the relative probability of upconverting a photon for a given delay. When the relative delay is too high or too low (the input and escort pulses have little or no temporal overlap) the probability of conversion is low. As the relative delay approaches maximum overlap (at

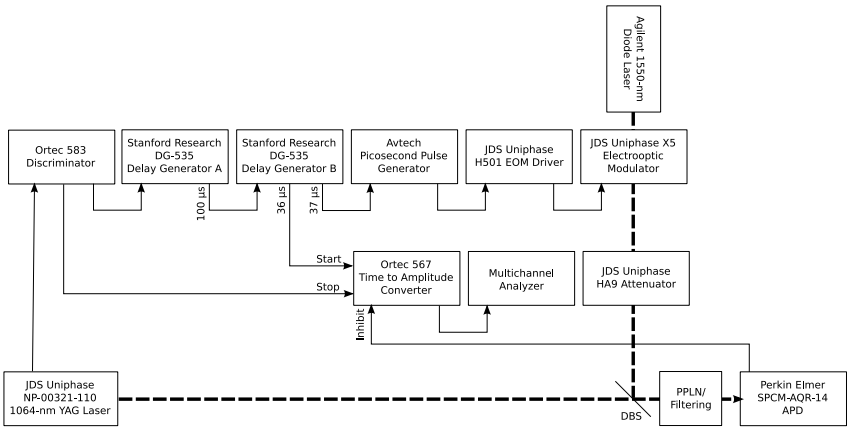

Figure 5.3: Layout of the scheme of indirect Rabi oscillation measurements. The solid lines represent electrical signals, while the dashed lines are laser beam paths. An escort and an input pulse are applied to the crystal with a random relative delay between the pulses. When we fail to detect an upconverted photon for a particular pulse, that delay is recorded and a histogram (Figure 5.4) is made, showing the relative probability that a delay will *not* result in an upconverted photon.

about 600 ps on Figure 5.4) the probability of conversion increases. However, the probability achieves local maxima at 400 and 800 ps, and then decreases for delays less than 200 ps away from the maximum overlap. We conclude that when the signal pulse approaches the peak of the escort, it completely converts to the higher energy state, and then partially converts back to the initial state. This local minimum at the peak escort intensity indicates that we are able to Rabi oscillate photons by performing rotations slightly beyond the π pulses which merely convert to the higher energy and stop. This approach, while clearly demonstrating the Rabi-like nature of upconversion, has limited application in quantum information, because we are dependent on the pulse shape and pulse-to-pulse jitter of the escort laser to apply different rotations to the frequency state of a photon. It would be much more useful to directly control the escort intensity and observe photons oscillating between the two frequency states.

5.4 Direct Observations of Rabi Oscillations

We obtained direct control of the escort intensity applied to the input pulse by delaying the escort pulse in a Harriot cell (Section 3.3). When the Nd:YAG laser produces a pulse, we detect it using an AEPX-65 fast photodiode before directing it into a 200-ns long Harriot cell, which stores the photon for sufficient time that we can generate a 1544-nm pulse which is synchronized directly to the current escort pulse, and not to the previous one, as was the case in the indirect Rabi measurement (Section 5.3). The photodiode signal triggers a pair of delay generators in series (Stanford Research DG-535), which trigger two

Time (ns)	Event
0	Escort pulse
10	Ortec 583 CFD triggers
20	Ortec 567 TAC "stops" previous cycle
100,020	DG-535 delay generator A signals to DG-535 B
136,020	DG-535 B signals TAC
136,030	Ortec 567 TAC "starts"
137,020	DG-535 B signals pulse generator
137,030	Avtech pulse generator produces 200-ps pulse
137,040	H301 EOM Driver pulses
137,050	X5 Fires
σ + 137,050	Escort pulse
σ + 137,055	APD Inhibits TAC
σ + 137,060	Ortec 583 CFD triggers
σ + 137,070	Ortec 567 TAC "stops"

Table 5.1: Timing chronology in indirect Rabi observation

series EOMs. By controlling the programmable delays on the DG-535 delay generators we can cause each input pulse to arrive at the crystal simultaneously with its corresponding escort (Section 3.5). Since the temporal overlap is always fixed at the maximum, we can directly control the escort intensity that the input photon "sees" by simply attenuating the escort (Section 3.4).

We plot the number of upconverted photons for various escort intensities in Figure 5.5. The first peak has a conversion efficiency of about 98%, limited by the spatial mode overlap. To achieve high peak intensities, the escort was focused to a 220-μm spot, while the 1544-nm beam was focused to an 100-μm spot. Though the input was smaller than the escort, a small amount of the input photon extended beyond the central peak region of the escort, leading to reduced conversion. We also fit a (single free parameter) theoretical prediction obtained by integrating the field-evolution equations (Equations 1.7 and 1.8) and including the effect of the measured pulse shapes of the escort and input photons. The measured temporal profile of the input pulse (Figure 5.2) includes a long non-Gaussian tail due the device limitations of the EOM used to create it. This leads to an incomplete extinction in the first minimum ($\sim$2 μJ in Fig. 5.5), since not all of the input light falls within the peak intensity of the escort pulse.

The data clearly show the overconversion of the photons as they transition from 1544 to 630 and back to 1544 nm, and that we can directly control the conversion probability by varying the escort intensity. In this way, we can prepare quantum states that are arbitrary superpositions of the two frequency states: $\alpha|630\,\mathrm{nm}\rangle e^{-i\omega_{630}t} + \beta|1544\,\mathrm{nm}\rangle e^{-i\omega_{1544}t}$. We know of no other method to efficiently produce such non-degenerate photon states, which may have use in quantum networking protocols, e.g., protocols requiring coupling to stationary non-degenerate qubits, or in protocols where time-dependent qubits may be desirable. By invoking the polarization-dependence of the upconversion process,

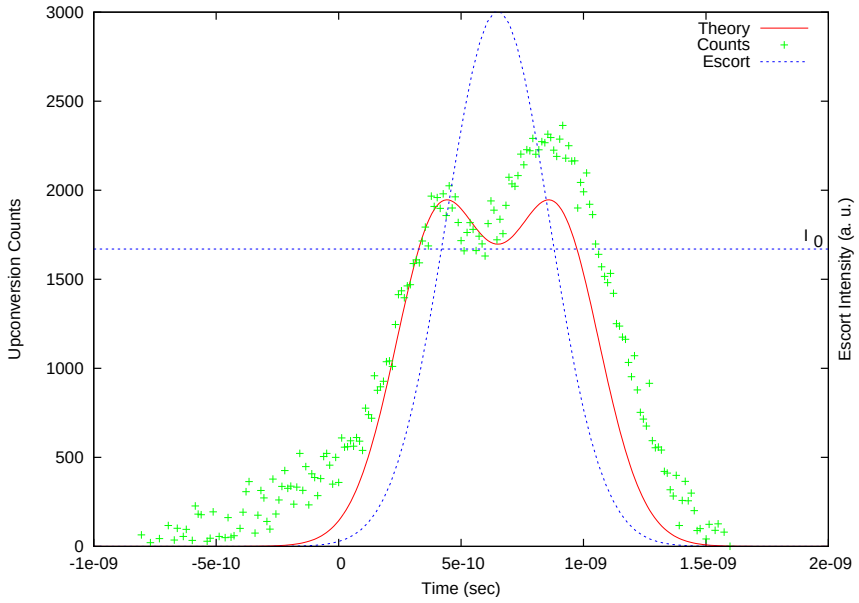

Figure 5.4: Indirect measurement of Rabi oscillations. Escort pulse shape along with its theoretical conversion profile obtained from a 400-ps input pulse. We record the relative input-escort delay of pulses that generated upconverted photons (calculated from subtracting events which did *not* upconvert from the background). This measurement is equivalent to the probability of conversion as the input pulse is swept across the escort pulse, and should be similar to the plotted theoretical prediction. The asymmetry of the data is likely due to a long escort tail which was not accounted for in the theoretical model of the escort. However, the salient feature of the graph–the two peaks–is present, indicating that overconversion is achieved.

even more complicated quantum states–residing in a larger Hilbert space–can be created.

5.5 Atom Simulator

If we look at the phase matching conditions for a periodically poled nonlinear crystal (Equations 1.5 and 1.10) we notice that for a given crystal with poling period Λ, and initial input (λ_i), escort (λ_e), and output (λ_o) wavelengths, if we shift the input wavelength a small amount (δ) to λ_i' and solve for the corresponding λ_e' and λ_o' for the same Λ, we find that the phasematched λ_e' will be shifted from λ_e by $\sim -(\lambda_e/\lambda_i)\delta$, whereas λ_o' will be very close to λ_o for small δ.

Using our experimental parameters of λ_i=1550 nm, λ_e=1064 nm, λ_o=631 nm, and Λ=11.4 μm, we calculate that for every nm of shift in λ_i, λ_o shifts by 1/30 nm (Figure 5.6). However, since the bandwidth of a 1-nm channel at 1550 nm is equal to a 0.4-nm band at 631 nm, we find we can have ∼12 distinguishable input states, which all have phasematched output states with significant overlap.

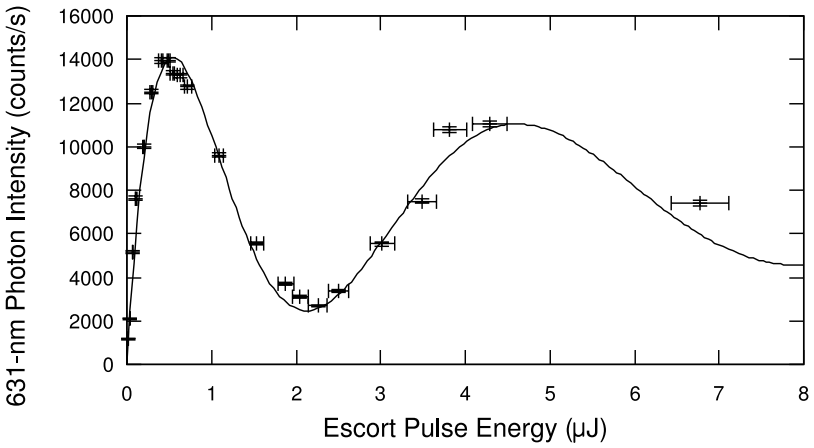

Figure 5.5: The Rabi oscillation-like nature of upconversion (Eqn. 1.9) is demonstrated by measuring the rate of upconverted photons for increasing escort-pulse intensities. The imperfect visibility is well modeled (solid line) by the precise pulse shapes. Visibility is mostly limited by the extent to which the 1544-nm pulse is temporally and spatially smaller than the escort pulse. The prediction was scaled in the pulse-energy direction due to inability to measure the absolute peak escort intensity to better than a factor of 2; however, predicted and measured pulse energies agree to that level.

By combining various input and escort beams we can achieve complex interactions that simulate Rabi oscillations, Raman transitions, and other quantum operations which are characteristic of a multilevel atom. For example, the system we have in place should be able to simulate an atom with 13 levels (1 ground state plus 12 excited states). These can be made to interact with each other by applying a combination of the 12 corresponding escort wavelengths. Figure 5.7 illustrates the correspondence between the multilevel upconversion system and the simulated atom.

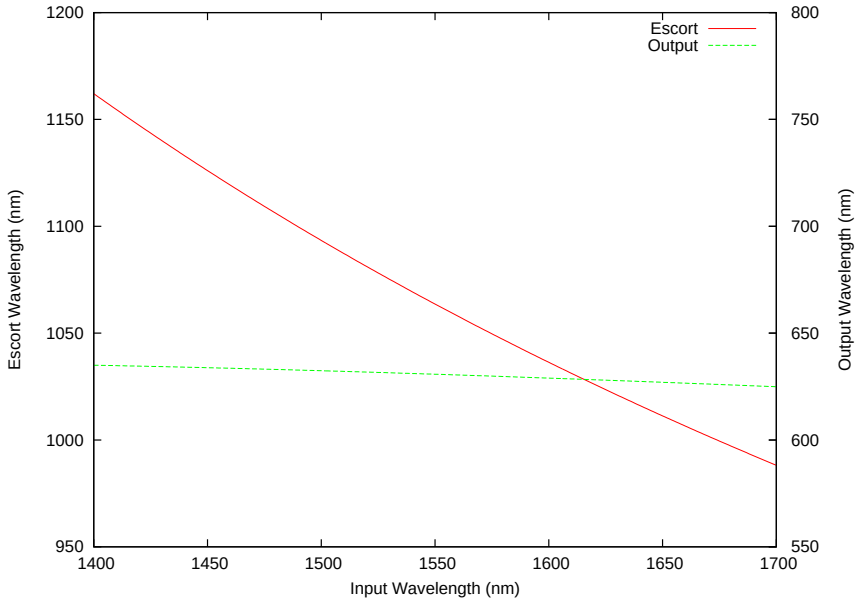

Figure 5.6: Dependence of phasematched escort and output wavelengths vs. input wavelength for constant crystal poling period (here assumed to be $\Lambda = 11.4$ μm). The output wavelength curve is plotted on an axis that is merely shifted and not scaled from the escort curve. This is to illustrate the relatively flat dependence of the output curve as compared to the escort curve.

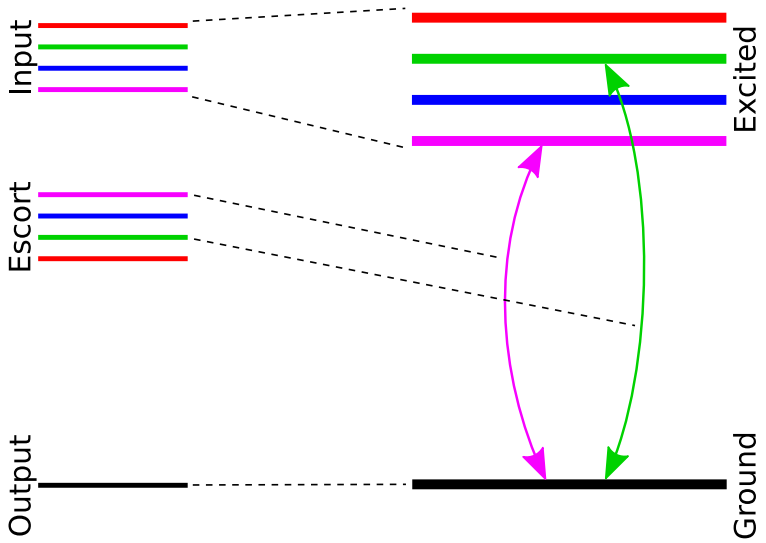

Figure 5.7: Multiple overlapping Rabi oscillations can be used to model the dynamics of a multilevel atom. Several pairs of input and escort wavelengths simultaneously phasematch with a single output wavelength. The escort beams act on the input beams as driving radiation fields act on the electronic structure of an atom. The input wavelengths are analogous to the excited states of the atom, while the output state is analogous to the ground state. By combining various escort wavelengths in a single crystal, we can create photons in complex nondegenerate superposition states.

6 Upconversion Switching

6.1 Introduction

The advent of telecommunication dense wave-division multiplexing systems (DWDM) that can transmit terabits of data per second has created a demand for optical switches capable of routing such optical signals. In order to fully harness the potential of high-speed optical networking, we require a switch which has low loss, low latency, transparency, and which can be easily frequency multiplexed to allow interoperation with DWDM systems. Here[1] we show that optical switches based on frequency upconversion [34] can fulfill this demand. Upconversion-based switching may also have advantages over other types of switching such as electrooptic [35], cascaded non-linear [36], and Kerr cross-phase modulation [37].

By upconverting a signal beam from the initial frequency to an intermediate state and back to the initial frequency (see Section 5.2) we may selectively apply a π-phase shift to the converted frequency and polarization. By combining this phase-modulation with various types of interferometers (e.g., Mach-Zehnder, Sagnac, etc.), we can create a class of intensity modulators which have several unique properties that are advantageous for telecommunications switching applications, including wavelength selectivity, bias-free operation, and robustness against thermal fluctuations.

6.2 Theory of Upconversion Phase Modulation

By solving the reduced non-linear field equations (equations 1.7 and 1.8), we can solve for the state as a function of position z in the crystal as the state converts from ω_i to ω_o:

$$|out\rangle = e^{i\phi_i}\cos(\alpha z)|\omega_i\rangle + e^{i(\phi_e+\phi_i+\pi/2)}\sin(\alpha z)|\omega_o\rangle, \tag{6.1}$$

where ϕ_i and ϕ_e are the input and escort phases, and α is a constant that depends on the experimental parameters. The evolution is effectively a Rabi oscillation between the input and output frequencies, controlled by the strength of the escort field. If we choose the crystal length to be $L = \pi/\alpha$ (i.e., a "2π-

[1] Sections in this chapter reproduced from [33]

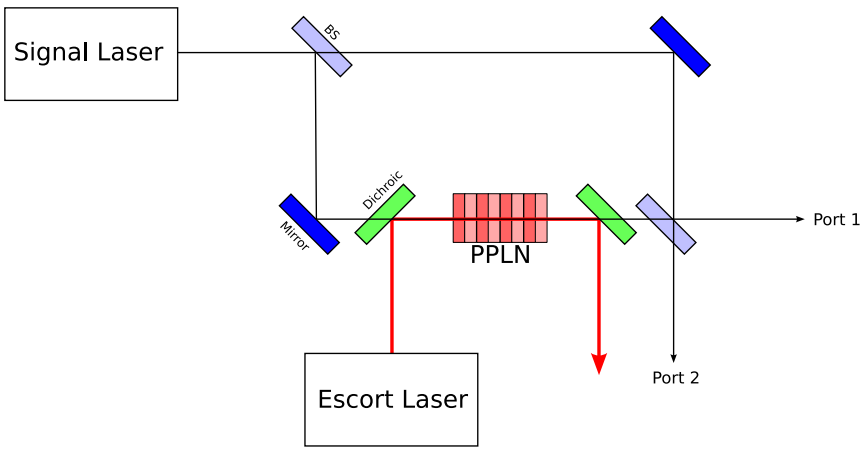

Figure 6.1: Design of basic upconversion switch using a Mach-Zehnder interferometer. A signal laser beam is sent through a balanced interferometer with a non-linear crystal (e.g., PPLN) in one arm. When an escort beam is passed through the crystal, collinearly with the signal, a π-phase shift is acquired by the signal, switching it from Port 1 to Port 2.

pulse"), then our final output state will be

$$|out\rangle = -e^{i\phi_i}|\omega_i\rangle, \tag{6.2}$$

which is equal to our original input state with a π-phase shift applied.

6.3 Mach-Zehnder Switch

Once we have the ability to apply π-phase shifts to our input beam, we may construct a switch by building an interferometer around the phase-modulator (Figure 6.1). The input light enters a Mach-Zehnder interferometer, which has a non-linear crystal and an appropriately phase-matched escort beam in one arm. If the interferometer is balanced and no escort is applied, then all of the input light will exit out Port 1. If the escort light is turned on, the input signal will upconvert to the higher frequency, then downconvert back to its initial frequency, acquiring a π-phase shift. The resulting modified interference condition on the exit beam splitter will cause the light to leave the interferometer out of Port 2.

6.4 Polarization Switch

In practice, the Mach-Zehnder design is somewhat difficult to implement in bulk materials, since it is very sensitive to thermal drift of the crystal, and requires mode-matching the two paths to a high-level of indistinguishability after one beam has passed through the crystal and the other has not. While we require temperature stabilization of the PPLN crystal to achieve phase-matching,

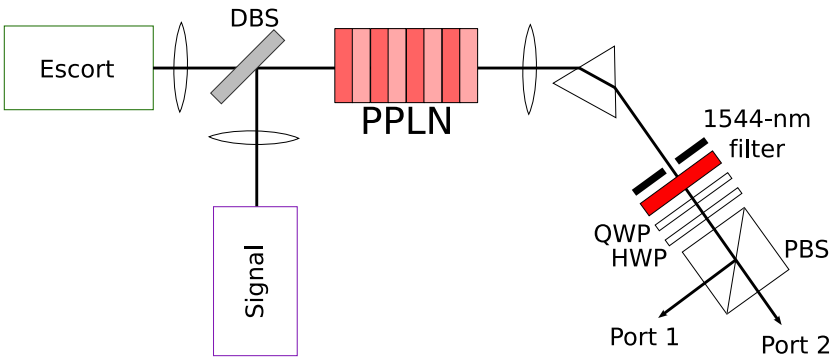

Figure 6.2: A diagonally polarized signal is passed through a non-linear crystal phase-matched for upconversion with an escort laser. The signal is filtered, and then passed though two waveplates and a PBS so that it exits out Port 1. When the escort beam is turned on, a π-phase shift is applied to the vertical component of the signal, switching it from Port 1 to Port 2.

this temperature tolerance is generally much greater than the temperature stability tolerance to require that the phase fluctuation due to the temperature-dependent index of refraction and thermal expansion of the crystal be much less than 2π. We could consider using an upconversion system based on quasi-phasematching of ordinary polarizations instead of extraordinary, as the former have much smaller temperature dependence on their refractive index; however, the nonlinear coefficients of these processes are significantly smaller, and therefore not useful for frequency conversion.

A better alternative to partially address this stability requirement is to construct a half-wave polarization modulator. We implemented a variant of the switch, where instead of having two separated interferometer arms, we used two polarizations in the same spatial mode (Fig. 6.2). Since both polarizations pass through the crystal–though only one polarization is upconverted–they both see a temperature-dependent index of refraction and the net phase is partially canceled out. In addition, because both paths travel though the same length of crystal, the Gaussian beams profiles evolve together, freeing us of the requirement to mode-match the two paths, which was necessary in the Mach-Zehnder design.

In our experiment we used a 1544-nm telecommunications laser diode [Agilent 81663A] to provide a signal beam with a peak power of $\sim$10 mW, which was focused inside of our crystal to a spot size of 70 μm. The signal was switched using a 1064-nm ND:YAG passively Q-switched escort laser with a repetition rate of 44 kHz, pulse width of 600 ps, and average power of 500 mW (JDS Uniphase DNP-150010-000 DualChip NanoPulse Laser). The escort was focused onto a somewhat larger spot size of 250 μm. The increased size allows the signal to observe a relatively constant escort field over the width of the signal. We used a 4.5-cm Periodically Poled Lithium Niobate (PPLN) crystal with an 11.4-μm

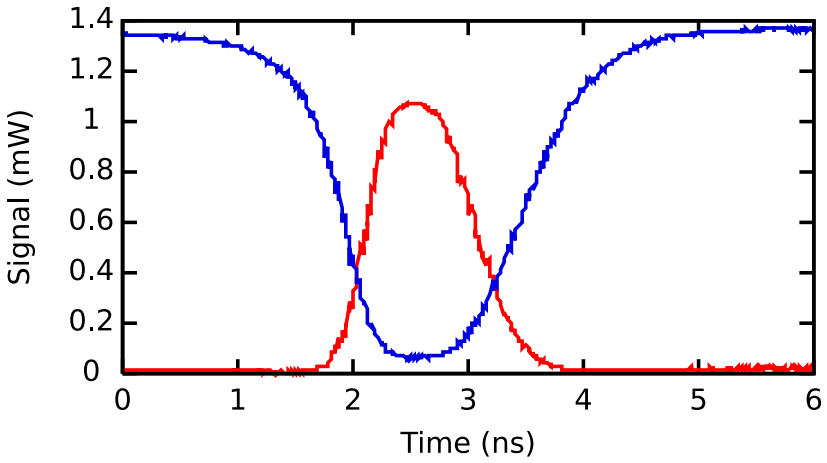

Figure 6.3: Data collected from the polarization-based upconversion switch. A 1544-nm signal was modulated with a 600-ps wide 1064-nm pulse in 4.5-cm PPLN crystal. The extinction is ∼20 dB and the transmission is about 70%. To average out the noise on the photodetector, each trace is a composite of 16 escort pulses.

poling period (HC Photonics Custom Multigrating PPLN Crystal) as our nonlinear medium. When heated to 70 °C, this crystal was quasi-phase matched for sum-frequency generation: 1544 nm + 1064 nm → 630 nm.

We combined our diagonally polarized signal with our vertically polarized escort on a dichroic beam splitter and passed both beams though the crystal. After the crystal, a dispersion prism and a 1500-nm high-pass filter (ThorLabs FEL1500) were used to separate the signal from the escort light. A quarter-wave plate (QWP) and half-wave plate (HWP) were used to negate the intrinsic phase difference between the H and V polarization components of the signal traveling through the birefringent crystal, and to rotate the signal to horizontal polarization, which then passed though exit Port 1 of the polarizing beam splitter (PBS). During the escort pulse interval, the vertical component of the signal in the crystal acquires an additional π-phase shift, causing the crystal to act like an additional HWP. Now when the signal reaches the exit PBS it will be vertically polarized and will exit Port 2. We can measure the switching performance either by placing detectors in both ports of the PBS, or by using a detector on one port, and observing the output for two positions of the HWP separated by 45°. Using the latter technique, Figure 6.3 shows the signals transmitted through each port during a switching cycle.

With this system we have achieved 20 dB of extinction in Port 2 and 12 dB of extinction in Port 1, with 0.7 dB of loss in Port 2 and $<$ 0.3 dB of loss in Port 1. The extinction ratio is mostly limited by spatial-mode mismatch, and therefore would be greatly improved by a waveguide implementation. The ∼400-ps 10%-90% switching time was limited by the Q-switched pulse width of the escort laser. By using a faster escort laser, much faster switching times

should be realizable. The switching speed is also limited by the acceptance bandwidth of the crystal, however,

$$\Delta\lambda = \frac{2\lambda\Lambda}{\pi L}, \tag{6.3}$$

and so faster switching requires shorter crystals, which in turn require higher escort intensities.

Next we consider the effect of temperature drifts on the PPLN crystal. For a 4.5-cm PPLN crystal, we calculate using the temperature-dependent Sellmeier index coefficients for congruent lithium niobate [38] that the Mach-Zehnder will vary 420° of phase per °C, while the polarization design only varies 370° of phase per degree. We constructed a polarization-based switch and observed fluctuations over the course of a few minutes of ∼20° of phase. This indicates temperature fluctuations on the order of 0.05° inside the crystal. Our crystal is temperature stabilized using a resistive oven and PID-based temperature controller (HC Photonics model TC-038) that has a precision of 0.1 °C. We determined that the source of our observed fluctuations was internal to the oven and controller by thermally isolating the oven from the room and repeating the phase-stability measurement. The oven was enclosed in a 30 cm cubic box which was constructed from a layer of corrugated cardboard on the inside, then 25 mm of acoustic/thermal insulating foam, and finally a 1 mm hard rubber exterior. The oven was left on inside of the insulating box for 24 hours to equilibriate, after which, the phase fluctuations were measured again. We found similar phase fluctuations and concluded that the fluctuations were not caused by variations in the environment, but hysteresis in the temperature controller. This problem can be mitigated by changing the control constants on the controller (the controller is driven by a proportional-integral-differential (PLD) integrated circuit) to lessen the proportional response characteristic, thereby obtaining a more consistent temperature at the expense of longer equilibrium times. Alternately, we could replace the feedback-based temperature controller with a low-noise current supply. This would provide a very steady temperature, but require tedious empirical determination of the current required to yield the correct phasematching temperature.

6.5 Frequency Multiplexing

After demonstrating fast and transparent switching, we also investigated the possibility of multiplexed switching. Since the π-phase shift is only applied to signals that are phase-matched to the switching escort beam, we are able to switch only a very narrow range of wavelengths while leaving the remaining wavelengths unaltered. This has applications in DWDM (dense wave-division multiplexing) systems where it may be desirable to switch out a single frequency channel. To investigate this we used the setup described in Figure 6.2, varied the

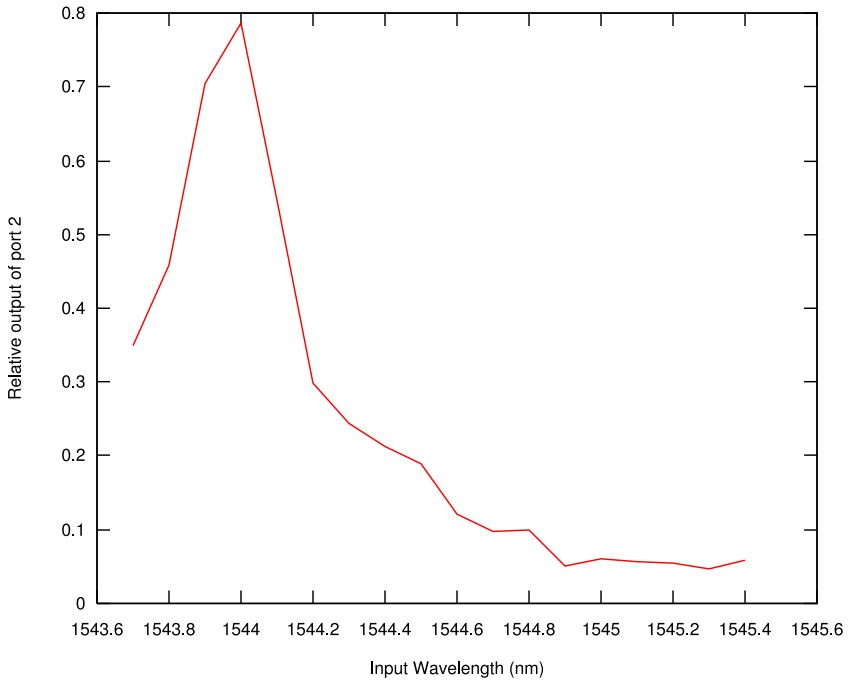

Figure 6.4: Data showing the wavelength selectivity of the upconversion switch, which therefore allows for frequency multiplexing. A 4.5-cm PPLN crystal and a 0.15-nm wide escort produce a 0.3-nm wide acceptance bandwidth. Nearby frequencies are unaltered. Transparency is limited to about 80% due to imperfect modematching between the escort and the signal.

input signal wavelength, and kept the escort wavelength constant. Our system was temperature-tuned for perfect quasi-phase-matching at 1544.0 nm, and we swept our input wavelength from 1543.7 nm to 1545.4 nm. We then measured the transmission of Port 2 as a function of wavelength and found a full width at half maximum (FWHM) switching bandwidth of 0.3 nm (Figure 6.4). This can be controlled by varying the length of the crystal and the bandwidth of the escort beam: shorter (longer) crystal and broader (narrower) escort bandwidth leads to broader (narrower) switching bandwidth.

One can easily envision a more flexible and general switch, where N independently controllable escort beams are used to control N different signal wavelengths. If the set of escort and signal wavelengths are spaced far enough apart so as not to phasematch with any other pair, activating some subset of the escort beams would switch only the corresponding set of signals, thus realizing a multi-frequency channel switch using only a single crystal.

6.6 Bias-Free Sagnac Switch

While the polarization-based switch has less temperature dependence than the Mach-Zehnder design, it is still susceptible to temperature stability requirements

tighter that those required for phase-matching. Both of these designs, however, require biasing to compensate for the phase difference between the two paths (either two spatial modes or two polarizations). Biasing in the Mach-Zehnder design can be achieved by applying an electrically induced index change, either in the same arm as the PPLN or in a non-linear crystal placed in the opposite arm of the interferometer, similar to the way in which electrooptic switches are biased. With the polarization case, the biasing was accomplished by setting the quarter- and half-wave plates to compensate for the extra phase difference caused by the birefringence of the crystal. In either case, switching performance requirements dictate that a dither-and-feedback circuit be used to hold a quadrature point, increasing complexity and limiting contrast.

We can eliminate this problem entirely by taking advantage of the fact that, unlike electrooptic switches, the phase is only applied to a beam which is co-propagating with the escort beam; a counter-propagating beam will not see a phase shift. This can be viewed as a weak time-reversal symmetry breaking (only the signal is time reversed), allowing us to implement a Sagnac design for the switch (Figure 6.5).

A horizontally polarized signal is transmitted through a polarizing beam splitter and a QWP which rotates the signal into right-circular polarization. The signal is then split using a 50/50 beam splitter, so one half travels clockwise around the interferometer and the other half travels counter-clockwise. The escort applies a π-phase shift to the (co-propagating) clockwise beam, while the counter-clockwise beam is counter-propagating to the escort and therefore not affected. If the escort is off, the signal (now left-circular after having undergone three reflections) exits the interferometer along the path from which it came. The HWP rotates the signal to vertical polarization before it reflects off the PBS, passes through a HWP to become horizontally polarized again, and leaves the switch through Port 1. If the escort is on, the interference condition on the beam splitter is reversed, and the signal leaves though Port 2 after the final QWP rotates it back to horizontal polarization. To upconvert both the horizontal and vertical components of the circularly polarized light inside of the interferometer, we require two upconversion crystals with perpendicular optic axes, and a diagonally polarized escort. Since both paths (clockwise and counter-clockwise) have to pass though the same crystals with each polarization, there is no need for any bias control. The system is self-stabilizing, as any index change caused by temperature instability will identically affect both paths. Such a bias-free switching configuration only needs to be temperature stabilized to the level required for phase-matching.

6.7 Other Implementations

By utilizing frequency upconversion we have demonstrated fast, transparent, efficient, multiplexable, bias-free optical switching suitable for classical and quan-

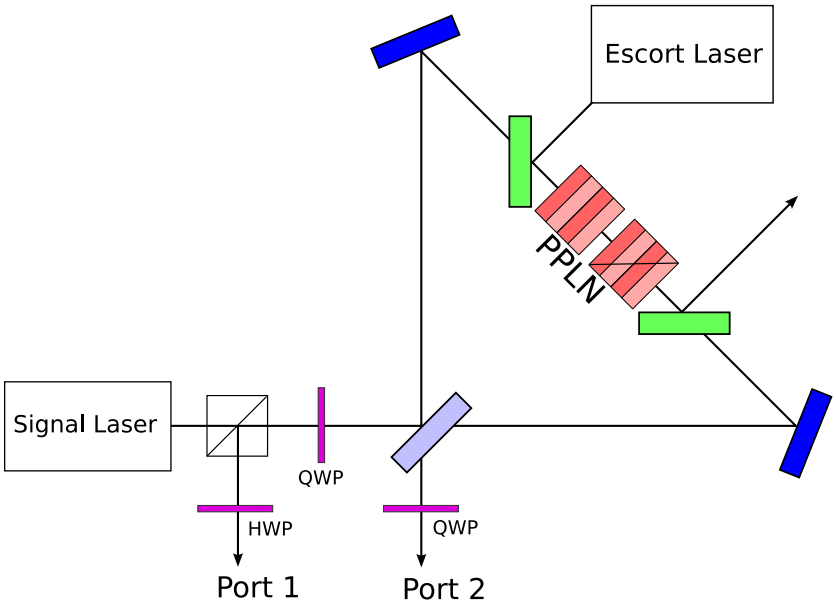

Figure 6.5: Design of bias-free upconversion switch using a Sagnac design. Since only the signal co-propagating with the escort beam acquires a phase, modulating the escort beam will shift the interference of the interferometer at the beam splitter and control whether the signal exits at Port 1 or Port 2.

tum communications. While we have focused on $\chi^{(2)}$ non-linear processes, the techniques could be generalized to $\chi^{(3)}$-based upconversion systems. Where high efficiency upconversion is possible [39], the concomitant π-phase shift necessary for switching can be obtained. This technique can also be used in waveguide-based integrated optical systems, where the decreased mode volume of the waveguide would dramatically lower the requirements for escort power [16].

A upconversion.scm

```
;; Routines for doing upconversion calculations
(define-module (sig upconversion))

(use-modules (ice-9 optargs)
             (sig math)
             (sig science)
             (sig macros)
             (sig math)
             (sig optics)
             (sig non-linear-optics)
             (sig data-handling))

;; Print a list of 4 wavelengths, l1, l2, l3, and Lambda from l1, l2
;; and Temp
(define-public (get-qpm l1 l2 temp)
  (let* ((l3 (get-generated-wavelength l1 l2))
         (L (get-ppln-period-temp l1 l2 temp)))
    (list l1 l2 l3 L temp)))

;; Finds the appropriate temperature based on l1 l2 and L
(define-public (get-temp l1 l2 L)
  (let ((l3 (get-generated-wavelength l1 l2)))
    (car (find-zeros (lambda (temp)
                       (let ((n1 (PPLN-index temp l1))
                             (n2 (PPLN-index temp l2))
                             (n3 (PPLN-index temp l3)))
                         (deltaK (list n3 n1 n2 1) (list l3 l1 l2 L))))
                     0 200))))

;; Get the crystal length from various parameters
(define-public (get-crystal-length l1 l2 temp E2)
  (let* ((l3 (get-generated-wavelength l1 l2))
         (w1 (lambda->omega l1))
         (w2 (lambda->omega l2))
```

```
         (w3 (lambda->omega l3))
         (n1 (PPLN-index temp l1))
         (n3 (PPLN-index temp l3))
         (dQeff (* (/ 2 pi) PPLN-dQ)))
    (/ (sqrt (/ (* pi pi n1 n3 c c) (* w1 w3 dQeff dQeff E2 (conj E2)))) 2)))

;; Find the peak escort field for a given system
;; This happens to have the same functional form as the crystal length,
;; so we just borrow that code.
(define-public (get-E2 l1 l2 temp len)
  (get-crystal-length l1 l2 temp len))

;; Find proper focusing given power and length
(define-public (find-waist l1 l2 power len temp)
  (car (find-zeros (lambda (waist)
                     (- (get-crystal-length
                         l1 l2 temp
                         (power->Epeak power waist
                                       (PPLN-index temp l2))) len))
                   1e-6 10e-3)))

;; Calculate phase mismatch
(define-public (deltaK indexes wavelengths)
  (* 2 pi (apply - (map / indexes wavelengths))))

;; Poling function
(define-public ((poling Lambda dQ) x)
  (if (even? (inexact->exact (floor (/ x (/ Lambda 2)))))
      dQ (* -1 dQ)))

;; differentials for explicit poling (dQ inverts every Lambda/2)
(define-public (make-upcon-derivs-poled lambda1 lambda2 Lambda temp)
  (let* ((lambda3 (get-generated-wavelength lambda1 lambda2))
         (w1 (lambda->omega lambda1))
         (w2 (lambda->omega lambda2))
         (w3 (lambda->omega lambda3))
         (n1 (PPLN-index temp lambda1))
         (n2 (PPLN-index temp lambda2))
         (n3 (PPLN-index temp lambda3))
         (dK (deltaK (list n3 n1 n2) (list lambda3 lambda1 lambda2)))
         (dQ (poling Lambda PPLN-dQ)))
    (lambda (x E1 E2 E3)
      (list
```

```
       (/ (* I w1 (dQ x) E3 (conj E2)
             (exp (* I dK x))) (* n1 c)) ; dE1/dx
       (/ (* I w2 (dQ x) E3 (conj E1)
             (exp (* I dK x))) (* n2 c)) ; dE2/dx
       (/ (* I w3 (dQ x) E1 E2
             (exp (* -1 I dK x))) (* n3 c)))))) ; dE3/dx

;; differentials with Quasi-Phase Matching factored into deltaK and dQ
(define-public (make-upcon-derivs lambda1 lambda2 Lambda temp)
  (let* ((lambda3 (get-generated-wavelength lambda1 lambda2))
         (w1 (lambda->omega lambda1))
         (w2 (lambda->omega lambda2))
         (w3 (lambda->omega lambda3))
         (n1 (PPLN-index temp lambda1))
         (n2 (PPLN-index temp lambda2))
         (n3 (PPLN-index temp lambda3))
         (dK (deltaK (list n3 n1 n2 1)
                     (list lambda3 lambda1 lambda2 Lambda)))
         (dQ (* (/ 2 pi) PPLN-dQ)))
    (lambda (x E1 E2 E3)
      (list
       (/ (* I w1 dQ E3 (conj E2) (exp (* I dK x))) (* n1 c)) ; dE1/dx
       (/ (* I w2 dQ E3 (conj E1) (exp (* I dK x))) (* n2 c)) ; dE2/dx
       (/ (* I w3 dQ E1 E2 (exp (* -1 I dK x))) (* n3 c)))))) ; dE3/dx

;; differentials for explicit poling (dQ inverts every Lambda/2)
;; And we assume that dE2/dx = 0 (non-delpetion regime)
;; This is the condensed form since it only uses 2 variables
;; instead of 3
(define-public (make-upcon-derivs-poled-cond
                lambda1 lambda2 Lambda temp E2)
  (let* ((lambda3 (get-generated-wavelength lambda1 lambda2))
         (w1 (lambda->omega lambda1))
         (w2 (lambda->omega lambda2))
         (w3 (lambda->omega lambda3))
         (n1 (PPLN-index temp lambda1))
         (n2 (PPLN-index temp lambda2))
         (n3 (PPLN-index temp lambda3))
         (dK (deltaK (list n3 n1 n2) (list lambda3 lambda1 lambda2)))
         (dQ (poling Lambda PPLN-dQ)))
    (lambda (x E1 E3)
      (list
       (/ (* I w1 (dQ x) E3 (conj E2)
```

```
             (exp (* I dK x))) (* n1 c)) ; dE1/dx
       (/ (* I w3 (dQ x) E1 E2
             (exp (* -1 I dK x))) (* n3 c))))))) ; dE3/dx

;; differentials with Quasi-Phase Matching factored into deltaK and dQ
(define-public (make-upcon-derivs-cond lambda1 lambda2 Lambda temp E2)
  (let* ((lambda3 (get-generated-wavelength lambda1 lambda2))
         (w1 (lambda->omega lambda1))
         (w2 (lambda->omega lambda2))
         (w3 (lambda->omega lambda3))
         (n1 (PPLN-index temp lambda1))
         (n2 (PPLN-index temp lambda2))
         (n3 (PPLN-index temp lambda3))
         (dK (deltaK (list n3 n1 n2 1) (list lambda3 lambda1 lambda2 Lambda)))
         (dQ (* (/ 2 pi) PPLN-dQ)))
    (lambda (x E1 E3)
      (list
       (/ (* I w1 dQ E3 (conj E2) (exp (* I dK x))) (* n1 c)) ; dE1/dx
       (/ (* I w3 dQ E1 E2 (exp (* -1 I dK x))) (* n3 c))))))) ; dE3/dx

;; Analytic upconversion expression
(define* (upconvert-analytic l1 l2 L t len E1 E2
                             #:key (condensed #t) #:allow-other-keys)
  (let* ((l3 (get-generated-wavelength l1 l2))
         (n1 (PPLN-index t l1))
         (n2 (PPLN-index t l2))
         (n3 (PPLN-index t l3))
         (dQ (* (/ 2 pi) PPLN-dQ))
         (w1 (lambda->omega l1))
         (w2 (lambda->omega l2))
         (w3 (lambda->omega l3))
         (A (/ (* w1 dQ (conj E2)) (* n1 c)))
         (B (/ (* w3 dQ E2) (* n3 c)))
         (a (deltaK (list n3 n1 n2 1) (list l3 l1 l2 L)))
         (g (sqrt (+ (* 4 A B) (sq a))))
         (E3 (/ (* B E1
                   (exp (* -1 I a len 0.5)) 2 I (sin (* g len 0.5))) g))
         (E1 (/ (* E1
                   (exp (* I a len 0.5))
                   (- (* g (cos (* g len 0.5)))
                      (* I a (sin (* g len 0.5))))) g)))
    (if condensed (list E1 E3) (list E1 E2 E3))))
```

```
;; integrate and return the final E3 Intensity.

(define*-public
  (upconvert lambda1 lambda2 Lambda temp len input escort
             #:key (poled #f) (condensed #t) (analytic #t) (store #f)
             #:allow-other-keys #:rest rest)
  (if (and analytic (or store poled)) (set! analytic #f))
  (if analytic
      (upconvert-analytic lambda1 lambda2 Lambda temp
                          len input escort #:condensed condensed)
      (let ((derivs (cond ((and poled condensed)
                           (make-upcon-derivs-poled-cond
                            lambda1 lambda2 Lambda temp escort))
                          ((and (not poled) condensed)
                           (make-upcon-derivs-cond
                            lambda1 lambda2 Lambda temp escort))
                          ((and poled (not condensed))
                           (make-upcon-derivs-poled
                            lambda1 lambda2 Lambda temp))
                          ((and (not poled) (not condensed))
                           (make-upcon-derivs
                            lambda1 lambda2 Lambda temp)))))
        (apply odeint 0 len
               (if condensed (list input 0) (list input escort 0))
               derivs #:store store rest))))


(define-public (escort-profile t)
  (if (< t 0.9e-9)
      (exp (/ (- (sq (- t 0.65e-9))) (sq 0.3e-9)))
      (* 1.92621 (exp (* -1.5e9 t)))))
```

B process-pulse.scm

```
#!/usr/bin/guile -s
!#

(use-modules (sig data-handling))
(use-modules (sig math))
(use-modules (sig signals))

(let ((cl (command-line)))
  (if (not (or (= (length cl) 4) (= (length cl) 6)))
      (begin
        (display (string-append
                  "Usage: process-pulse.scm [-f low-pass-freq]"
                  "trace.txt dark.txt normal.txt\n"))
        (exit)))
  (let* ((lpf (equal? "-f" (cadr cl)))
         (low-pass-freq (if lpf (string->number (caddr cl)) 0.1))
         (trace (list-ref cl (if lpf 3 1)))
         (dark (list-ref cl (if lpf 4 2)))
         (normal (list-ref cl (if lpf 5 3))))
    (comment-file trace)
    (comment-file dark)
    (let* ((points (file->points trace))
           (points2 (inexact->exact
                     (round (pow 2 (floor (/ (log points) (log 2)))))))
           (trace-coarse-v (file->vector trace))
           (dark-coarse-v (file->vector dark))
           (xrange-coarse (file->xrange trace))
           (trace-fourier-v (vector-truncate trace-coarse-v points2))
           (dark-fourier-v (vector-truncate dark-coarse-v points2))
           (xrange-fourier (* xrange-coarse (/ points2 points))))
      (coarse-grain! trace-coarse-v 5)
      (coarse-grain! dark-coarse-v 5)
      (low-pass-filter! trace-fourier-v low-pass-freq)
      (low-pass-filter! dark-fourier-v low-pass-freq)
      (let* ((normal-coarse-v (vector-subtract
```

```
                    trace-coarse-v dark-coarse-v))
      (normal-fourier-v (vector-subtract
                         trace-fourier-v dark-fourier-v))
      (f-coarse (data->function
                 normal-coarse-v xrange-coarse 'center))
      (f-fourier (data->function
                  normal-fourier-v xrange-fourier 'center))
      (area-coarse1 (integrate f-coarse -1e-9 1e-9))
      (area-coarse2 (integrate f-coarse -2e-9 2e-9))
      (area-fourier1 (integrate f-fourier -1e-9 1e-9))
      (area-fourier2 (integrate f-fourier -2e-9 2e-9))
      (error (abs (/ (- area-coarse2 area-coarse1)
                     area-coarse2)))
      (extinct-coarse
       (* (/ 10 (log 10))
          (log (abs (/ (* (f-coarse 0) 2e-9)
                       (- area-coarse2 area-coarse1))))))
      (pulse-vis-coarse
       (* (/ 10 (log 10))
          (log (abs (/ area-coarse1
                       (- area-coarse2 area-coarse1))))))
      (extinct-fourier
       (* (/ 10 (log 10))
          (log (abs (/ (* (f-fourier 0) 2e-9)
                       (- area-fourier2 area-fourier1))))))
      (pulse-vis-fourier
       (* (/ 10 (log 10))
          (log (abs (/ area-fourier1
                       (- area-fourier2 area-fourier1)))))))
(vector->file normal
              "#Trace: " trace "\n"
              "#Background: " dark "\n"
              "#XRange: " (number->string xrange-fourier) "\n"
              "#Area [-1ns:1ns]: "
              (number->string area-coarse1) "\n"
              "#Area [-2ns:2ns]: "
              (number->string area-coarse2) "\n"
              "#Error: " (number->string error) "\n"
              "#Coarse Extinction Ratio (dB): "
              (number->string extinct-coarse) "\n"
              "#Coarse Pulse Visibisity (dB): "
              (number->string pulse-vis-coarse) "\n"
              "#FFT Extinction Ratio (dB): "
```

```
(number->string extinct-fourier) "\n"
"#FFT Pulse Visibisity (dB): "
(number->string pulse-vis-fourier) "\n"
"#CG Trace, CG Dark, CG Normal, F Trace,"
" F Dark, F Normal\n"
trace-coarse-v
dark-coarse-v
normal-coarse-v
trace-fourier-v
dark-fourier-v
normal-fourier-v)))))
```

C error-analysis.scm

```
#!/usr/bin/guile
!#

(use-modules (sig math)
             (sig data-handling)
             (sig macros)
             (sig signals)
             (sig non-linear-optics)
             (ice-9 optargs))

(define (make-file-name file)
  (string-append "/g/home/sig/photons/data/rabi/dark-error/"
                 (if (number? file) (number->string file) file)
                 "-normal.txt"))

(define calc-error
  (let* ((files (map make-file-name '(1 2 3 4 5 6 7 8 9)))
         (functions (map file->function files))
         (averages (map (lambda (f)
                          (/ (integrate f 0 5e-9) 5e-9)) functions))
         (average (/ (apply + averages) (length averages))))
    (lambda (time)
      (let* ((errors (map (lambda (f)
                            (integrate (lambda (x) (- (f x) average))
                                       0 time)) functions))
             (average-error (/ (apply + errors) (length errors)))
             (rms (sqrt (apply + (map sq errors)))))
        rms))))
;    (display
;     (string-append
;      "RMS: " (number->string rms) "\n"))))

(function->file calc-error 0 5e-9
                (make-file-name "error-progression.txt"))
```

```
(define (error-function t)
  (+ (* 8e-8 t) (* 5e-13 (sqrt t))))

(error-function 2e-9)
```

D Noise from Crystal Damage

After a period of disuse, we noticed that when operating the upconversion-based single-photon detector, the background had increased significantly. Observation of the 4.5-cm PPLN crystal under a microscope (Figure D.1) revealed some discoloration on the entry and exit faces of the crystal. We characterized this noise source and found it to be highly polarized (Figure D.2), dependent on lateral position in the crystal (Figure D.3), and quadratically dependent on escort power (Figure D.4). We sent the crystal back to the manufacturer to be re-diced, and re-coated for anti-reflection at 1550/1064/631 nm. We retested for noise after the crystal had been reconditioned and found the background had returned to previous levels. We suspect that the damage was caused burn spots or photo-refractive damage at or near the ends of the crystal, and that these areas were fluorescing. The quadratic nature seems to suggest that either two-photon fluorescence (or fluorescence from the 532-nm second harmonic light) was at work, or that fluorescence photons at or near 1550 nm were upconverting in the crystal (a linear dependence on the fluorescence and a linear dependence on the upconversion yields a quadratic dependence on the escort power); however, the polarization measurement indicates most of the background was horizontally polarized, making the upconversion scenario unlikely.

Figure D.1: Photo taken under a microscope of the end of a damaged PPLN crystal. The discoloration of the first ∼1 mm is evident.

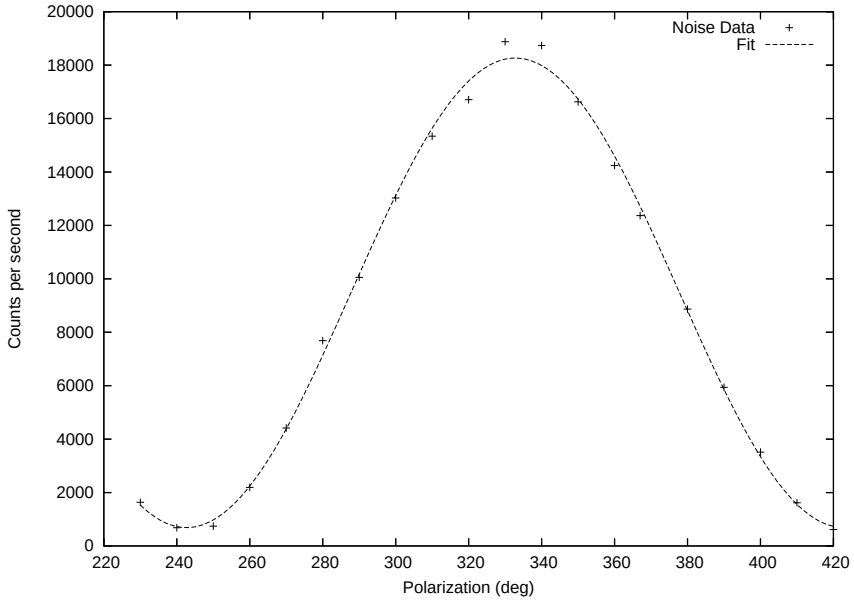

Figure D.2: Measurement of noise versus polarization. A fit reveals a polarization visibility of 93%, and is horizontally polarized.

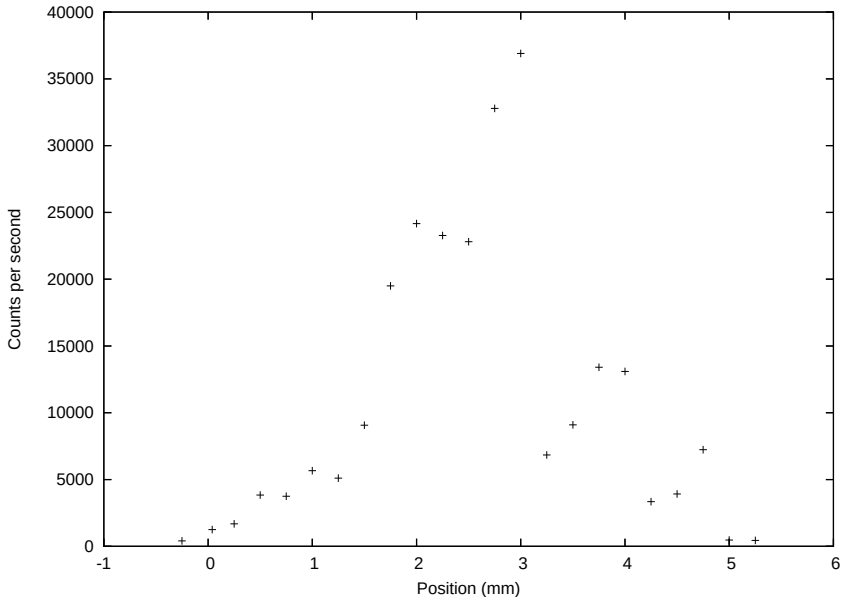

Figure D.3: Measurement of noise versus lateral position in the crystal. The noise peaks near the 11.4-μm channel that we use for upconversion. From this, it seems likely that the presence of the intense escort beam contributed to causing the damage, possibly through burning or photo-refractive damage.

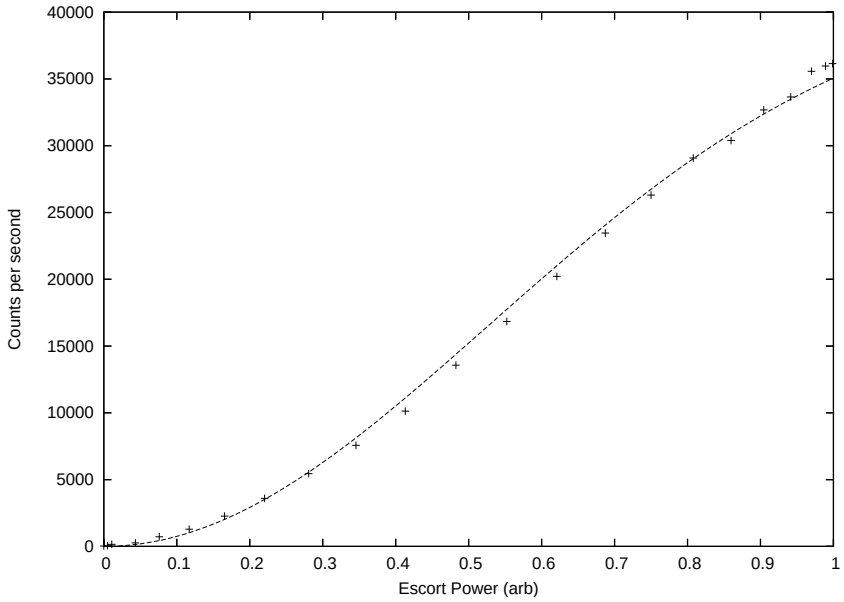

Figure D.4: Measurement of noise versus power. The fit shows a quadratic dependence on escort power, until the detector saturates near the pulse repetition rate at 44 kHz. The fit function is $N = 4200(1 - \exp(1.8I^2))$, where N is the number of background counts per second, and I is the fraction of maximum escort power used.

References

[1] P. Horowitz and W. Hill. *The Art of Electronics*. Cambridge University Press, New York, NY, 1989.

[2] J. A. Armstrong, N. Bloembergen, J. Ducuing, and P. S. Pershan. Interactions between light waves in a nonlinear dielectric. *Phys. Rev.*, 127:1918–1939, 1962.

[3] G. D. Boyd and D. A. Kleinman. Parametric interaction of focused gaussian light beams. *J. Appl. Phys.*, 39:3597–3639, 1968.

[4] J. E. Midwinter. Image conversion from 1.6 μm to the visible in lithium niobate. *Appl. Phys. Lett.*, 12:68–70, 1968.

[5] K. F. Hulme and J. Warner. Theory of thermal imaging using infrared to visible image up-conversion. *Appl. Opt.*, 11:2956–2964, 1972.

[6] T. R. Gurski, H. W. Epps, and S. P. Maran. Upconversion of broadband infrared spectra. *Appl. Opt.*, 17:1238–1242, 1978.

[7] R. Schanz, S. A. Kovalenko, V. Kharlanov, and N. P. Ernsting. Broad-band fluorescence upconversion for femtosecond spectroscopy. *Appl. Phys. Lett.*, 79:566–568, 2001.

[8] J. Warner. Spatial resolution measurements in up-conversion from 10.6 μm to the visible. *Appl. Phys. Lett.*, 13:360–362, 1968.

[9] F. V. Bright. Modern molecular fluorescence spectroscopy. *Appl. Spectroscopy*, 49:14A–19A, 1995.

[10] M. M. Abbas, T. Kostiuk, and K. W. Ogilvie. Infrared upconversion for astronomical applications. *Appl. Opt.*, 15:961–970, 1976.

[11] Rostislav V. Roussev, Carsten Langrock, Jonathan R. Kurz, and M. M. Fejer. Periodically poled lithium niobate waveguide sum-frequency generator for efficient single-photon detection at communication wavelengths. *Opt. Lett.*, 29:1518–1520, 2004.

[12] Marius A. Albota and F. N. C. Wong. Efficient single-photon counting at 1.55 μm by means of frequency upconversion. *Opt. Lett.*, 29:1449–1451, 2004.

[13] G. Giorgi, P. Mataloni, and F. De Martini. Frequency hopping in quantum interferometry: efficient up-down conversion for qubits and ebits. *Phys. Rev. Lett.*, 90:027902, 2003.

[14] Ketil Karstad, André Stefanov, Mark Wegmuller, Hugo Zbinden, Nicolas Gisin, Thierry Aellen, Mattias Beck, and Jérôme Faist. Detection of mid-ir radiation by sum frequency generation for free space optical communication. *Opt. and Lasers in Engineering*, 43:537–544, 2005.

[15] A. P. VanDevender and P. G. Kwiat. High efficiency single photon detection via frequency up-conversion. *J. of Mod. Opt.*, 51:1433–1445, 2004.

[16] Carsten Langrock, Eleni Diamanti, Rostislav V. Roussev, Yoshihisa Yamamoto, and M. M. Fejer. Highly efficient single-photon detection at communication wavelengths by use of upconversion in reverse-proton-exchanged periodically poled linbo$_3$ waveguides. *Opt. Lett.*, 30:1725–1727, 2005.

[17] Kyo Inoue, Edo Waks, and Yoshishisa Yamamoto. Differential phase shift quantum key distribution. *Phys. Rev. Lett.*, 89:037902, 2002.

[18] M. A. Nielsen and I. L. Chuang. *Quantum Computation and Quantum Information*. Cambridge University Press, Cambridge, U. K., 2000.

[19] Nicolas Gisin, Grégoire Ribordy, Wolfgang Tittel, and Hugo Zbinden. Quantum cryptography. *Rev. Mod. Phys.*, 74:145–195, 2002.

[20] Jianming Huang and Prem Kumar. Observation of quantum frequency conversion. *Phys. Rev. Lett.*, 68(14):2153–2156, Apr 1992.

[21] S. Tanzilli, W. Tittel, M. Halder, O. Alibart, P. Baldi, N. Gisin, and H. Zbinden. A photonic quantum information interface. *Nature*, 437:116–120, 2005.

[22] L. E. Myers, R. C. Eckardt, M. M. Fejer, R. L. Byer, W. R. Bosenberg, and J. W. Pierce. Quasi-phase-matched optical parametric oscillators in bulk periodically poled $LiNbO_3$. *J. Opt. Soc. Am. B*, 12:2102–2116, 1995.

[23] D. E. Browne and T. Rudolph. Resource-efficient linear-optical quantum computation. *Phys. Rev. Lett.*, 95:010501, 2005.

[24] R. J. Hughes, G. L. Morgan, and C. G. Peterson. Quantum key distribution over a 48-km optical fiber network. *J. Mod. Opt.*, 47:533–547, 2000.

[25] E. Knill, R. Laflamme, and G. J. Milburn. A scheme for efficient quantum computation with linear optics. *Nature*, 409:46–52, 2001.

[26] D. T. Pegg and J. Jeffers. Quantum nature of laser light. *J. Mod. Opt.*, 52:1835–1856, 2005.

[27] T. T. Basiev et al. Lithium flouride color center laser with an output energy of 100 j. *Sov. J. Quantum Electron.*, 15:745–746, 1985.

[28] T. T. Basiev et al. Application of large-aperture passive shutters from crystals LiF:F_2 for the generation of sub microsecond single pulses in neodymium-glass lasers with large-scale active elements. *Sov. Phys. Lebedev Inst. Rep.*, 1984(2):34–38, 1984.

[29] D. Stucki, N. Gisin O. Guinnard, G. Ribordy, and H. Zbinden. Quantum key distribution over 67 km with a plug&play system. *New J. Phys.*, 4:41.1–41.8, 2002.

[30] MagiQ Technologies http://www.magiqtech.com/.

[31] id Quantique http://www.idquantique.com/.

[32] J. J. Sakurai. *Modern Quantum Mechanics*. Addison-Wesley Publishing Company, Reading, Massachusetts, 1994.

[33] A. P. VanDevender and P. G. Kwiat. High-speed transparent switch via frequency upconversion. *Opt. Express*, 15:4677–4683, 2007.

[34] A. P. VanDevender and P. G. Kwiat. Quantum transduction via frequency up-conversion. *J. Opt. Soc. Am. B*, 24:295–299, 2007.

[35] Ed L. Wooten, Karl M. Kissa, Alfredo Yi-Yan, Edmond J. Murphy, Donald A. Lafaw, Peter F. Hallemeier, David Maack, Daniel V. Attanasio, Daniel J. Fritz, Gregory J. McBrien, and Donald E. Bossi. A review of lithium niobate modulators for fiber-optic communications systems. *IEEE J. Selected Topics in Quantum Electron.*, 6:69–82, 2000.

[36] Y. Baek, R. Schiek, and G. I. Stegeman. All-optical switching in a hybrid mach-zehnder interferometer as a result of cascaded second-order nonlinearity. *Opt. Lett.*, 20:2168–2170, 1995.

[37] Masahiko Jinno and Takao Matsumoto. Nonlinear sagnac interferometer switch and its applications. *IEEE J. Quantum Electron.*, 28:875–882, 1992.

[38] K. K. Wong, editor. *Properties of Lithium Niobate, EMIS Data Reviews Series No. 5*. INSPEC, London, 1989.

[39] D. Méchin, R. Provo, J. D. Harvey, and C. J. McKinstrie. 180-nm wavelength conversion based on Bragg scattering in an optical fiber. *Opt. Express*, 14:8995–8999, 2006.

Author's Biography

Aaron Pace VanDevender was born on June 15, 1979 in Albuquerque, NM. He graduated from the Massachusetts Institute of Technology in 2001 with a bachelor degree in physics (Course 8A), completing his senior thesis on atomic interferometry of rubidium under the supervision of Dr. Selim M. Shahriar. He is currently a doctoral candidate at the University of Illinois at Urbana-Champaign, working on quantum information and nonlinear optics with Paul G. Kwiat, and is also president of the Falling Illini Skydiving Club.